Ⓔ

Site Effects and Peak Ground Accelerations Observed in Guadalajara, Mexico, for the 9 October 1995 M_w 8 Colima–Jalisco, Earthquake

by M. Chavez,[*] S. Garcia, E. Cabrera, M. Ashworth, N. Perea,
A. Salazar, E. Chavez,[†] J. Saborio-Ulloa,[‡] and J. Saborio-Ortega

Abstract   On 3 June 1932, an M_s 8.2 shallow thrust subduction earthquake struck the Colima–Jalisco (CJ) region of Mexico at an epicentral distance of ∼250 km from Guadalajara, the second largest town in Mexico. The return period of these CJ earthquakes has been estimated from 77 to 126 years, which suggests the next is likely to occur between 2009 and 2058. As a step toward estimating the seismic hazard posed by potential M_s 8.2+ events on Guadalajara, we present a study consisting of the following: (1) the analysis of the strong ground motions recorded at Guadalajara on 11 free-field accelerographs for the CJ 9 October 1995 M_w 8 earthquake; (2) the analysis of the site effects in Guadalajara observed for this earthquake; and (3) the estimation of the spatial distribution of peak ground acceleration (PGA) in Guadalajara for this event. We propose, validate, and apply a recurrent neural network (RNN) technique to the recorded PGA. Important site effects were identified (using the horizontal-to-vertical and H/H$_{rocksite}$ techniques) on Guadalajara's sandy soil layers with thicknesses $h > 20$ m to the basaltic rock basement. The estimated PGAs in Guadalajara for the CJ 1995 earthquake varied from ∼2 to ∼27 cm/s^2 for soil layers with $h \leq 5$ m and $h > 50$ m, respectively. We expect the hybrid technique to obtain broadband synthetics (Chavez et al., 2011) and the proposed RNN methodology can be used to estimate Guadalajara's seismic hazard for M_w 8+ CJ scenario earthquakes.

Online Material: Figures of Fourier amplitude spectra, H/V and H/H spectral ratios, and signal-to-noise spectral ratios.

Introduction

The occurrence of large-magnitude, damaging earthquakes in the Colima–Jalisco (CJ) region in northwestern Mexico (Fig. 1a) has been documented (at least) since the sixteenth century (García-Acosta and Suárez Reynoso, 1996). For example, over the last 200 years, the following events occurred: 25 March 1806 (M_s 7.5), 3 May 1818 (M_s 7.7), 20 January and 16 May 1900 (M_s 7.6 and 7.1, respectively), 3 and 18 June 1932 (M_s 8.2 and 8, respectively), 30 January 1973 (M_s 7.3, M_w 7.6), 9 October 1995 (M_s 7.4, M_w 8), and 22 January 2003 (M_s 7.3, M_w 7.4). The estimated rupture areas for the events that have occurred in the CJ region since 1932 and of the Michoacan earthquake of the 19 September 1985

(M_s 8.1, M_w 8.01) are shown in Figure 1a (which includes the location of the profile shown in Fig. 1b). In Figure 1a, notice the large extent of the rupture surface of the 1932 M_s 8.2 event, compared with the corresponding smaller magnitude earthquakes, as well as some of the overlapping rupture areas.

The return period for earthquakes in the CJ region with $M_w/M_s \geq 8$ ranges from 77 to 126 years (Nishenko and Singh, 1987). Therefore, there is a non-negligible possibility of having a similar or larger magnitude event in this region of Mexico in the current time window (2009–2058).

The only strong ground motion records available at Guadalajara for $M_w \geq 8$ events are the ones obtained for the M_w 8 CJ 1995 event (hereafter CJ1995), a subduction, shallow depth, thrust mechanism earthquake with an epicentral distance of 240 km of Guadalajara (Fig. 1; Courboulex et al., 1997; Escobedo et al., 1998). Good-quality records were obtained for the CJ1995 event at 11 surface and 2 downhole stations of the Guadalajara Accelerographic Network (Fig. 2) deployed in 1992–1993 (Chavez, 1993, 1995). Therefore, to obtain reliable estimates of the seismic hazard and possible

---

  *Also at Scientific and Technology Facilities Council, Daresbury Laboratory, Daresbury Science & Innovation Campus, Warrington WA4 4AD, United Kingdom.
  †Also at Business School, Finance Department, Imperial College London, South Kensigton Campus, Tanaka Building, SW7 2AZ London, United Kingdom.
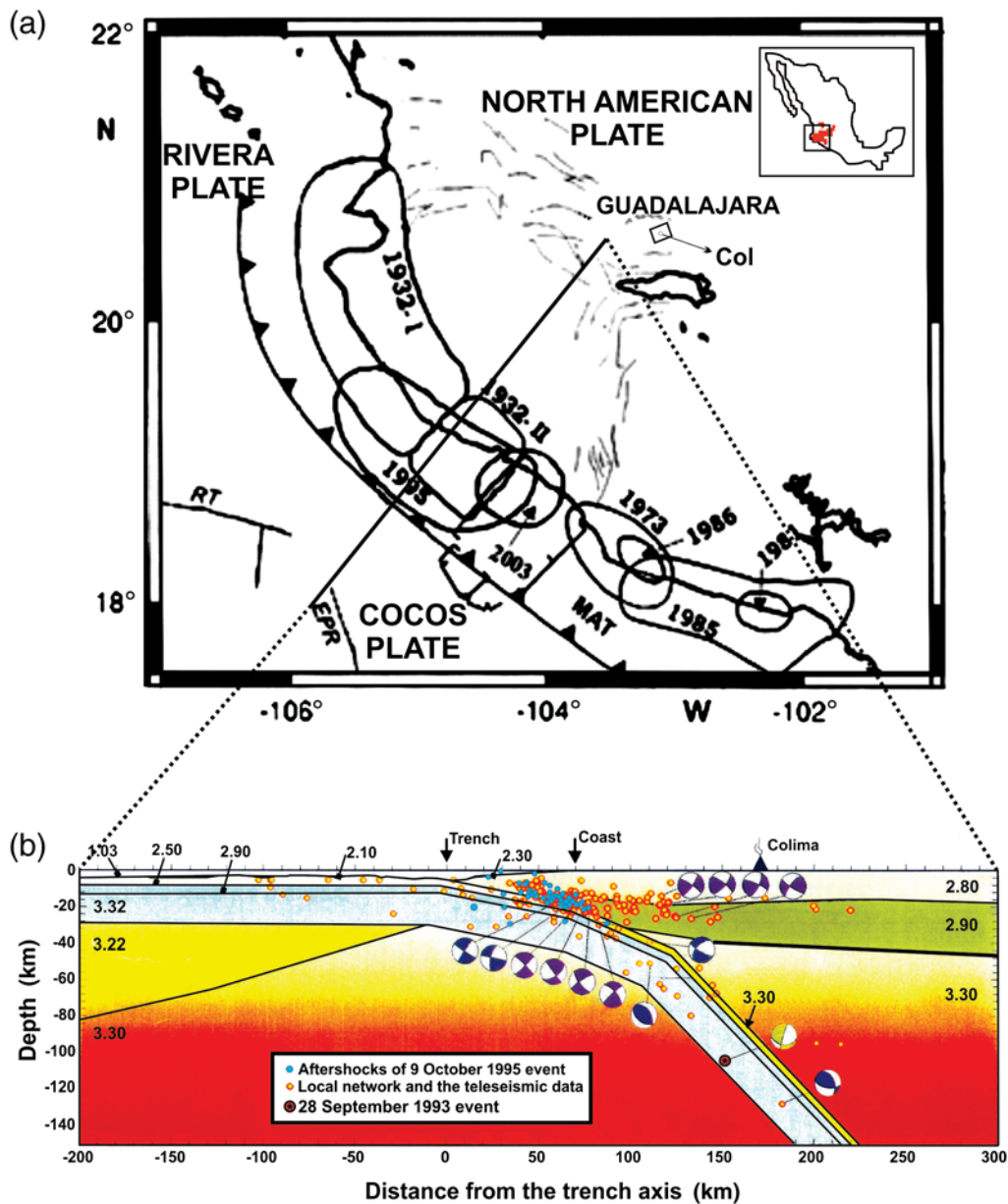 ‡Deceased (2011).

Figure 1.   (a) Location of the Colima–Jalisco (CJ) region in Mexico. Rupture areas for the 3 and 18 June 1932, 31 January 1973, 9 October 1995, 22 January 2003, and 19 September 1985 earthquakes. RT, Rivera trench; EPR, east Pacific rise; MAT, middle American trench. (Modified from Pacheco and Kostoglodov, 1999.) (b) Geological structure of the CJ region, including the densities (g/cm^3) of the Rivera (subducting) and North American (subducted) plates layers. (Adapted from Chavez et al., 2011.) The color version of this figure is available only in the electronic edition.

consequences for the Guadalajara metropolitan zone (the second largest town of Mexico; Instituto Nacional de Estadistica y Geografia [INEGI], see Data and Resources) posed by the possible occurrence in the CJ region of $M_w \geq 8$ earthquakes of the 1932 type, there is a need to generate synthetics (such as the ones obtained for the CJ1995 by Chavez et al., 2011) associated with this kind of plausible seismic scenario and to obtain the spatial distribution of their associated strong ground motion intensities in Guadalajara.

Taking the above into consideration, we present a study that includes: (1) the analysis of the strong ground motions

recorded at Guadalajara Accelerographic Network for the CJ1995 earthquake; (2) the analysis of the site effects in Guadalajara observed for this earthquake; and (3) the estimation of the spatial distribution (x, y) of the peak ground accelerations (PGA) in Guadalajara using recurrent neural network (RNN) techniques.

The first objective was achieved by processing and analyzing the time and frequency characteristics of the strong ground motions recorded at Guadalajara for the CJ1995 earthquake (event 2 in Table 1) and those recorded at JAR, COL$_{surface}$, and COL$_{rock}$ (downhole) stations for its largest
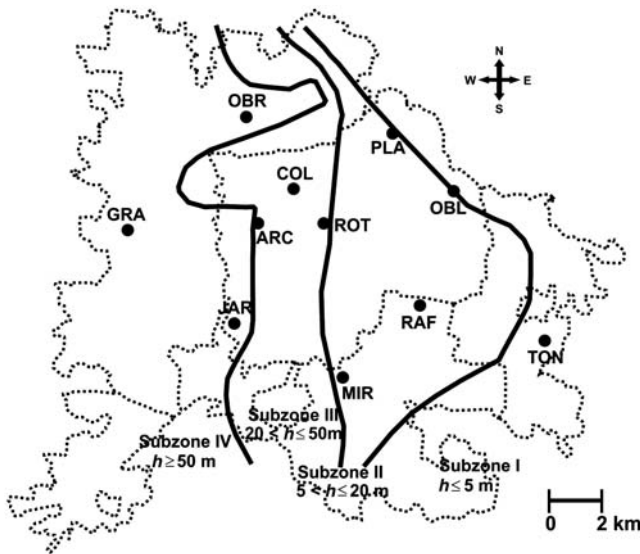
Figure 2. Location of the 11 free-field recording station sites of the accelerographic network of Guadalajara (in operation from 1992 to 1997). Geotechnical microzonation of Guadalajara in four subzones; h is the thickness of the sandy soil layers up to a competent basaltic rock. (Adapted from Chavez, 1995, 2000.)

M_w 5.75 foreshock (F) and M_w 5.92 aftershock (A), events 1 and 3 in Table 1, respectively. The analysis included a study of the probable existence of site effects at Guadalajara's recording station sites by obtaining the horizontal-to-vertical (H/V) spectral ratios at the 11 station sites and the transfer functions of 10 of the station sites, with respect to a rock site station, for the CJ1995 earthquake. For the estimation of the spatial (x, y) distribution of the PGA in Guadalajara, we propose, validate, and apply an RNN procedure to the recorded PGA.

We begin this paper with a discussion of the seismotectonics of the CJ region, the superficial geology of Guadalajara, and the main seismological characteristics of the CJ1995 earthquake. This is followed by the analysis of the recordings obtained at Guadalajara for the CJ1995 event and the study of the local site effects at Guadalajara by the computation of the H/V spectral ratios and of the transfer functions at the station

sites with respect to a reference superficial rock site of the recordings for the CJ1995 earthquake. We discuss the development, validation, and application of an RNN technique for the estimation of the spatial distribution of PGA in Guadalajara for the CJ1995 event and provide our main conclusions.

Seismotectonics of the Colima–Jalisco Region, the Superficial Geology of Guadalajara, and the 1995 Colima–Jalisco Earthquake

Seismotectonics of the Colima–Jalisco Region

The CJ region seismotectonics are basically related to the subduction of the Rivera and the Cocos plates beneath the North American plate (NOAM) in the northern part of the middle American trench in western Mexico (Fig. 1a). The age of the Rivera plate has been estimated between 10 and 15 million years (Klitgord and Mammericks, 1982; Kostoglodov and Bandy, 1995), and its rate of subduction below the NOAM plate is estimated to be only 2–5 cm/year (Kostoglodov and Bandy, 1995); however, between 1932 and 2009, this subduction process generated the two large earthquakes of 1932, as well as one in 1995 (Fig. 1a).

The geological structure of the subducting and continental plates in the CJ region is shown in Figure 1b. In this figure, the subducting slab has initial dip angles from ∼9° to ∼16° down to a depth of ∼20 km and then slowly increases to ∼50° at depths below 50 km. The Rivera plate consists of three layers (with densities of 2500, 2900, and 3320 kg/m³) and the upper mantle beneath it (density 3300 kg/m³). The continental crust consists of an upper layer (density 2800 kg/m³), a lower crustal layer (density 2900 kg/m³), the upper mantle beneath it (density 3300 kg/m³), and a thin sedimentary layer (density of 2300 kg/m³) in the continental slope zone (Bandy *et al.*, 1999). Based on borehole information and their own gravimetric study, Campos-Enriquez and Alatorre-Zamora (1998) suggested the existence of low density (2450–2780 kg/m³) superficial layers of rhyolitic tuffs and andesite, with thicknesses of 1–3 km, lying on a granite layer under and near Guadalajara (see Fig. 3).

Table 1
Source Parameters of Events 1–3 and Subevents 1–4 of the CJ1995
Earthquake (Chavez *et al.*, 2011)

Event	Depth (km)	Strike (°)	Dip (°)	Rake (°)	M_0 (N·m)	M_w
1 Foreshock	18	314	29	104	4.28×10^{17}	5.75
2 Mainshock	24	306	26	94	1.84×10^{20}	8.00
3 Aftershock	21	290	25	76	7.75×10^{17}	5.92
Subevent 1	28	320	28	98	4.39×10^{19}	7.02*
Subevent 2	31	286	25	84	4.92×10^{19}	7.09*
Subevent 3	19	338	25	119	4.13×10^{19}	7.04*
Subevent 4	20	282	26	75	5.00×10^{19}	7.10*

*Estimated from the moment magnitude M_0 values using $M_w = (\log M_0/1.5) - 10.7$ (Kanamori and Anderson, 1975).

Figure 3. Shallow crustal structure in the vicinity of Guadalajara. (Adapted from Campos-Enriquez and Alatorre-Zamora, 1998.)
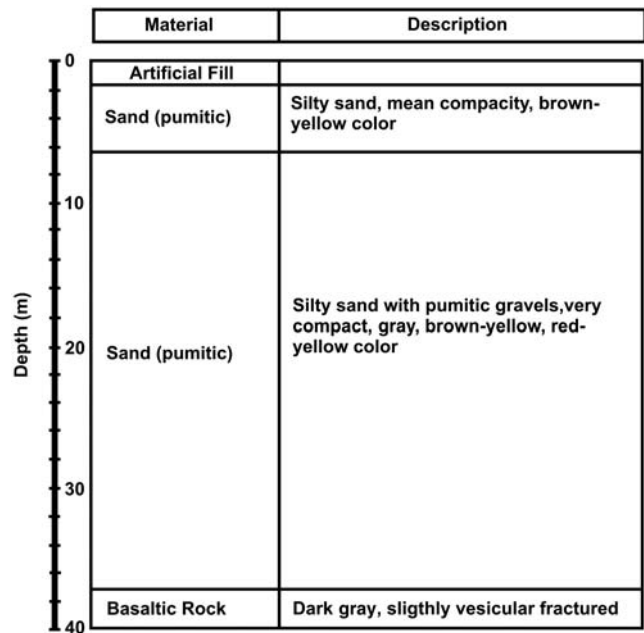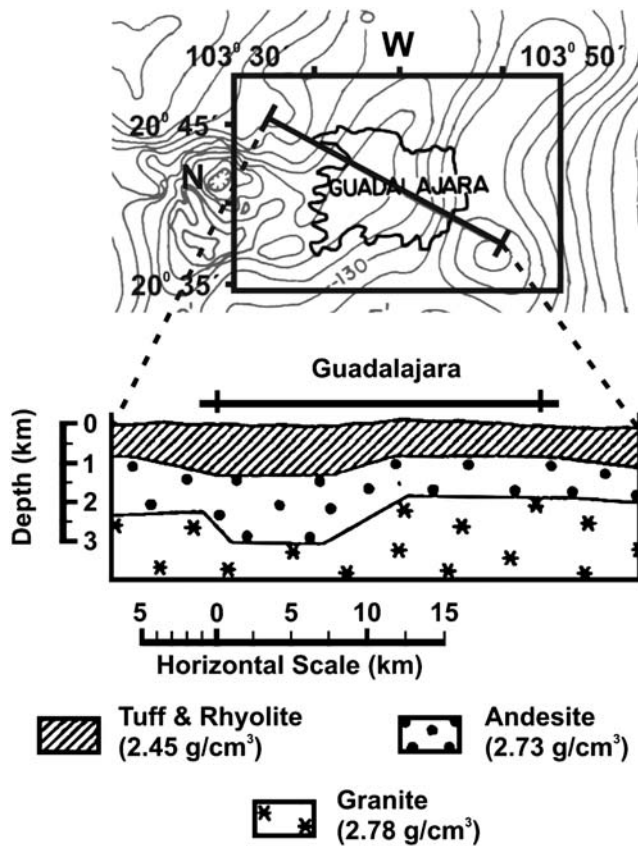

Figure 4. Typical superficial layering of pumitic sandy soils at Guadalajara, shown here for accelerographic station site COL; see Figures 2 and 5. (Adapted from Chavez, 1995.)

Superficial Geology of Guadalajara

Guadalajara is localized in the Guadalajara plain, which is located in the western part of the trans-Mexican volcanic belt (TMVB; Campos-Enriquez and Alatorre-Zamora, 1998). This region of the TMVB is mainly covered by Tertiary and Quaternary igneous rocks. The more recent rocks found in the Guadalajara plain are made of Quaternary pyroclastic flows and rhyolitic tuffs, and there are recent alluvial and lacustrine deposits filling the geomorphic and tectonic depressions found in its vicinity (Campos-Enriquez and Alatorre-Zamora, 1998). Based on the Bouguer anomaly and borehole data, these authors proposed that the shallow crustal structure in the neighborhood of Guadalajara consists of a granite basement located at ~2 to ~3 km depth, overlain by a layer of basaltic andesite of ~1 to ~2 km thickness, which in its turn is overlain by an ~1 km thick layer of tuff and rhyolite (Fig. 3).

The ~1 km layer of tuff and rhyolite in this case is covered by a thin layer of pumitic pyroclastic and alluvial material made of sand and gravel (i.e., a sandy pumitic material of varying thickness), as is exemplified by the typical geotechnical superficial layer of Guadalajara shown in Figure 4 (Chavez, 1995). Based on the detailed analysis of ~150 geotechnical borehole available data (similar to that in Fig. 4) distributed on the Guadalajara surface, the approximate depths of Guadalajara's sandy superficial soils layers to the competent basaltic rock (indicated in Figs. 2 and 5) were obtained (Chavez, 1995). Figure 5 also includes the approximate thicknesses of the sandy pumitic layers up to the basaltic rock layer under the 11 accelerographic station sites of Figure 2.

Figure 5 shows that the depth to rock of the sandy pumitic layers of Guadalajara increases smoothly and slowly from ~0.75 to ~100 m east–west directions (station sites TON and GRA) and from ~3 to ~50 m north–south directions (station sites MIR and OBR) (see also Fig. 2) (Chavez, 1995).

Taking these results into consideration, Chavez (1995, 2000), U. Saborio and O. Saborio proposed the geotechnical microzonation of Guadalajara shown in Figure 2, that is, four subzones, depending on the thicknesses h of Guadalajaras's sandy soil layers to competent basaltic rock. Subzones I–IV are categorized using $h \leq 5$ m, $5 < h \leq 20$ m, $20 < h \leq 50$ m, and $h > 50$ m, respectively.

The 1995 Colima–Jalisco Earthquake

The main seismotectonic results about the M_w 8 CJ1995 earthquake are synthesized in Figure 6 and Table 1 (Courboulex et al., 1997; Escobedo et al., 1998; Chavez et al., 2011). Four conclusions can be drawn: (a) The hypocenter coordinates of the CJ1995 mainshock (event 2 in Table 1) are 18.84° N, 104.55° W, and depth 24 km. (b) The CJ1995 rupture area was ~160 × ~90 km², which represents ~40% and ~100% of the rupture areas of the 3 and 18 June 1932 earthquakes, respectively (see Fig. 6). (c) The CJ1995 mainshock can be represented by the ruptures of four thrust mechanism subevents, identified by 1–4 in Table 1 and Figure 6. (d) Finally, the source mechanisms of events 1 and 3 and of
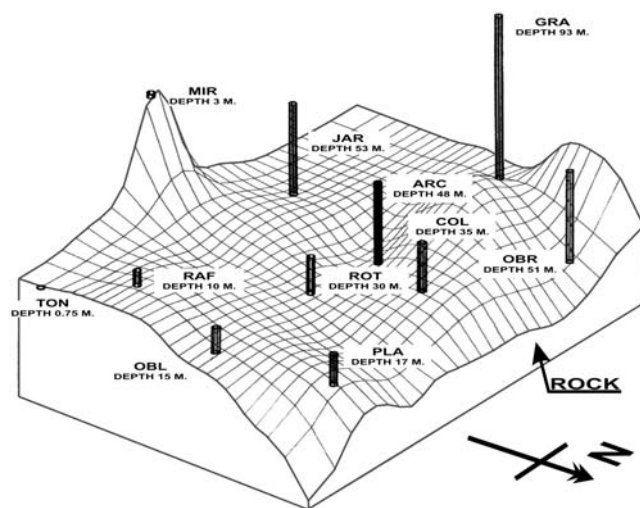
Figure 5. Depth to rock of the sandy superficial soils of Guadalajara and depths at the recording stations of the accelerographic network of Guadalajara. (Adapted from Chavez, 1995.).
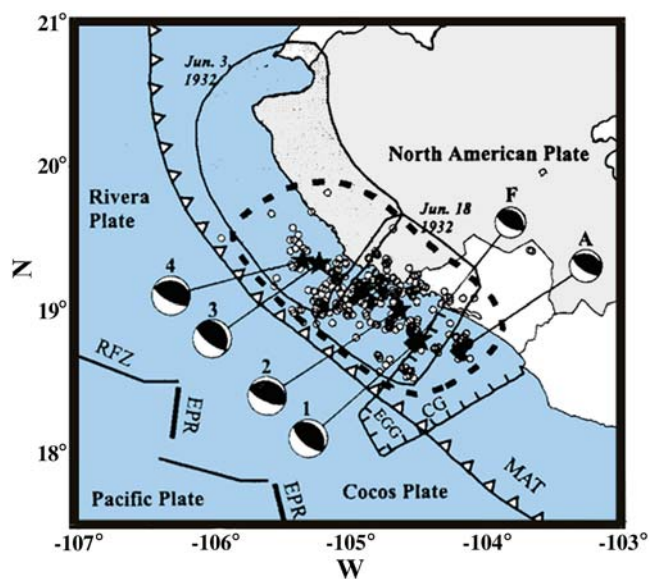

Figure 6. Rupture areas for the 3 and 18 June 1932 and 9 October 1995 earthquakes. Solid lines outline the rupture areas of the 3 and 18 June 1932 earthquakes. Epicentral locations and focal mechanisms are shown for (1) the 9 October 1995 event, with the largest foreshock (F) on 6 October 1995 and the largest aftershock (A) on 12 October 1995; the aftershock zone is outlined with a dashed line. The four subevents of the 9 October 1995 earthquake (1–4) are interpreted as the source for the main event. RFZ, Rivera fracture zone; EPR, east Pacific rise; EGG, El Gordo graben; CG, Colima graben; MAT, middle American trench. (Adapted from Escobedo *et al.,* 1998.) The color version of this figure is available only in the electronic edition.

the four subevents in Table 1 are similar to the average mechanism of the CJ1995 earthquake, that is, all of them are shallow-dipping, thrust-fault earthquakes, in agreement with the relative plate motions for the Rivera–NOAM and the Cocos–NOAM plate boundaries (see Fig. 1a).

Strong Ground Motions at Guadalajara of the 1995 M_w 8 Colima–Jalisco Earthquake and Its Largest M_w 5.75 Foreshock and M_w 5.92 Aftershock

Time and Frequency Domain Characteristics of the Accelerograms Recorded at Guadalajara for the M_w 8 CJ1995 Earthquake

For the CJ1995 earthquake, good quality, three-component strong ground motion records were obtained in the accelerographic network of Guadalajara (Figs. 2 and 5) equipped with surface and downhole Kinemetrics SSA-2 accelerographs (Chavez, 1993, 1995). At COL and JAR stations (Fig. 2), several additional records were obtained for events 1 and 3 in Table 1. None of the stations had a Global Positioning System, and, except for COL station (in which the surface and the downhole instruments were interconnected), all stations were autonomous. The individual clocks recorded the triggering time of an event based on the specific amplitude triggering level selected for the specific station; this level was chosen based on ambient vibration tests performed (in the urban environment of Guadalajara) at each of them. In all the accelerographs of the network, a 10 s pre-event recording time was set to guarantee the complete recording of the strong ground motions (until the amplitude of the signals were lower than their respective triggering level). The sampling of the recordings was set at 200 samples/s, the maximum acceleration they could record was of $\pm 2g$ ($g = 981$ cm/s^2), and the frequency response of the instruments was DC–50 Hz.

The processing of each recording required applying a baseline correction to a signal of interest and then filtering it using a band-pass filter with low and high cutoff frequencies of 0.01 and 50 Hz, respectively. The filtering was performed in the frequency domain by first applying a cosine taper of 5% of the total duration of the record, at the beginning and at the end of the signal, before computing its fast Fourier transform. A smoothing of the Fourier amplitude spectra of the signal also is carried out, by averaging six values of the latter, centered at each of the frequencies of the spectra.

For the analysis of the recordings at Guadalajara of the CJ1995 earthquake, the 11 station sites were grouped in three sets, depending on their soil layer depth (h) to the rock (see Figs. 2 and 5). Group 1 includes stations ARC, COL$_{surface}$, and ROT ($\sim 20 < h \leq \sim 50$ m); group 2 is formed by stations GRA, JAR, and OBR ($h > \sim 50$ m); and group 3 consists of stations OBL, PLA, RAF, MIR, and TON ($h \leq \sim 20$ m) (Figs. 2 and 5). Guadalajara's accelerographic network, which had a 100% recording success for the M_w 8 CJ1995 earthquake, stopped functioning in 1997 due to lack of interest and economical support of the local, state, and federal authorities, so the 2003 M_w 7.4 event was not recorded at Guadalajara.

In Figures 7–9, respectively, the west–east (W–E), north–south (N–S), and vertical (UD) accelerograms recorded at Guadalajara free-field stations for the CJ1995 mainshock are shown. In those figures, the values of the PGA retrieved
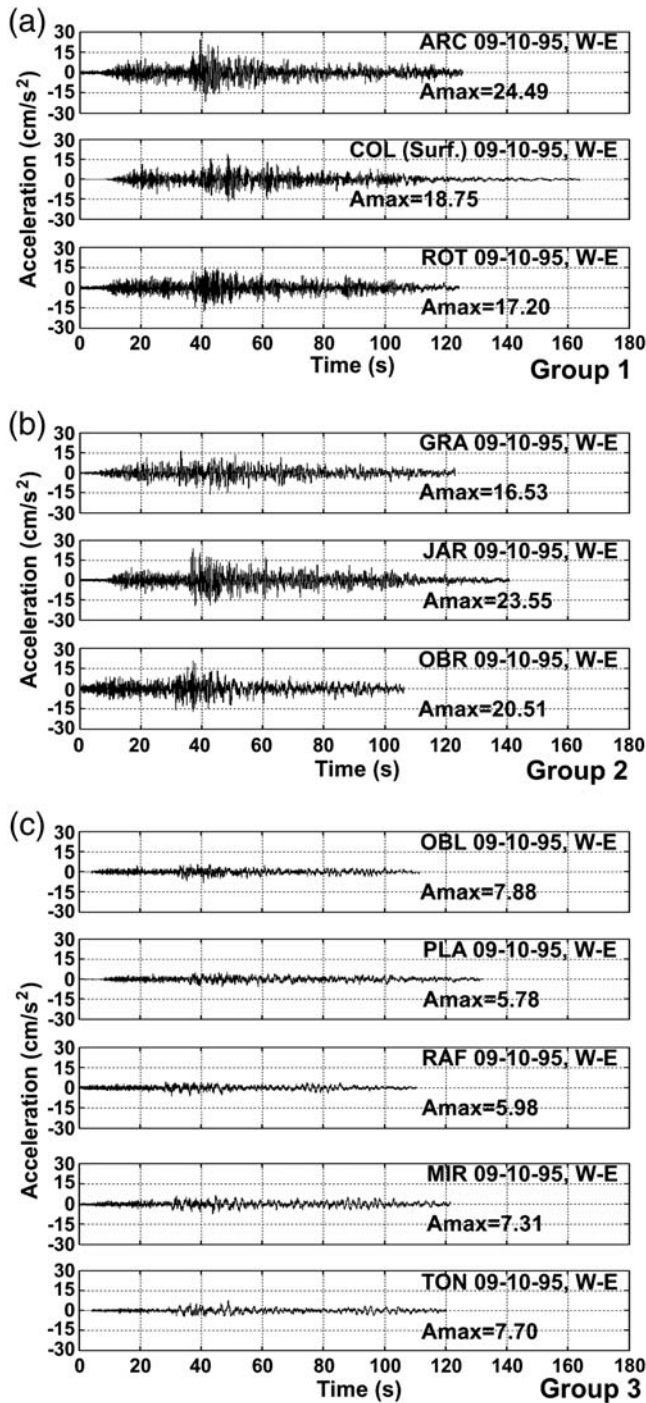
Figure 7. Accelerograms observed in the west–east (W–E) direction at Guadalajara's accelerographic network (see Figs. 2, 5) for the M_w 8 CJ1995 earthquake for stations groups (a) 1, (b) 2, and (c) 3.
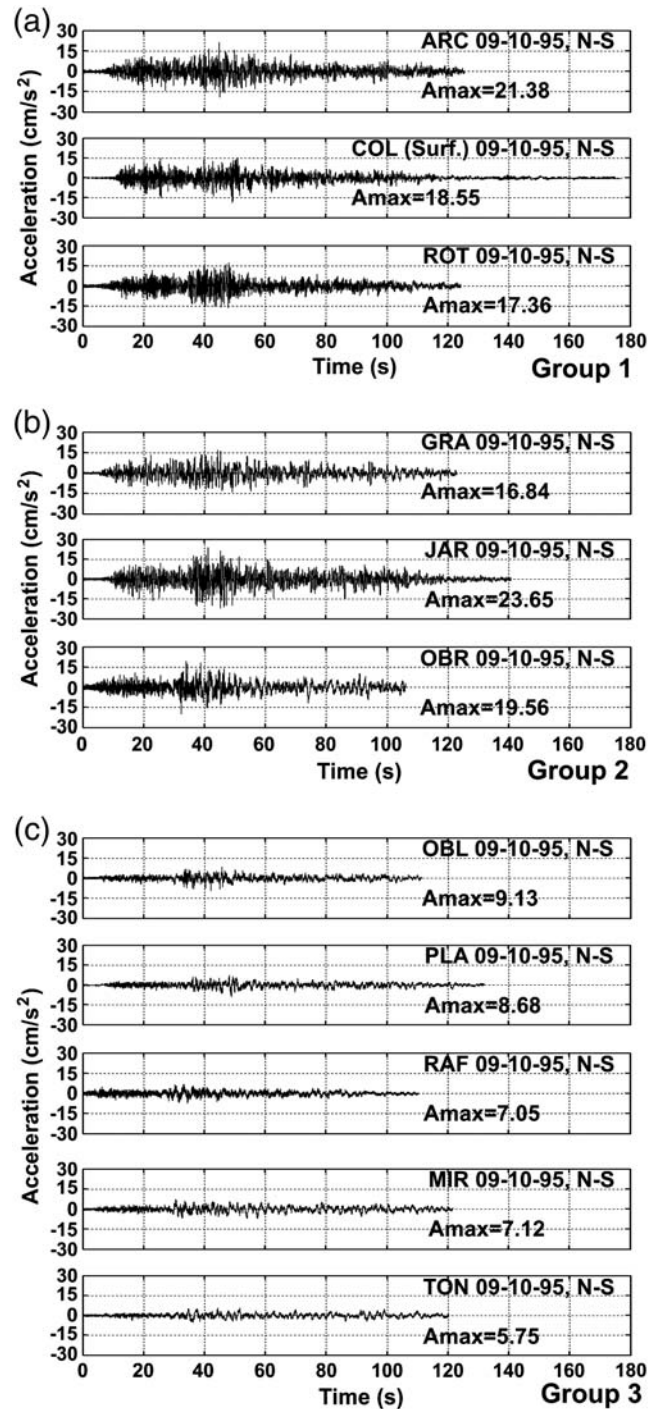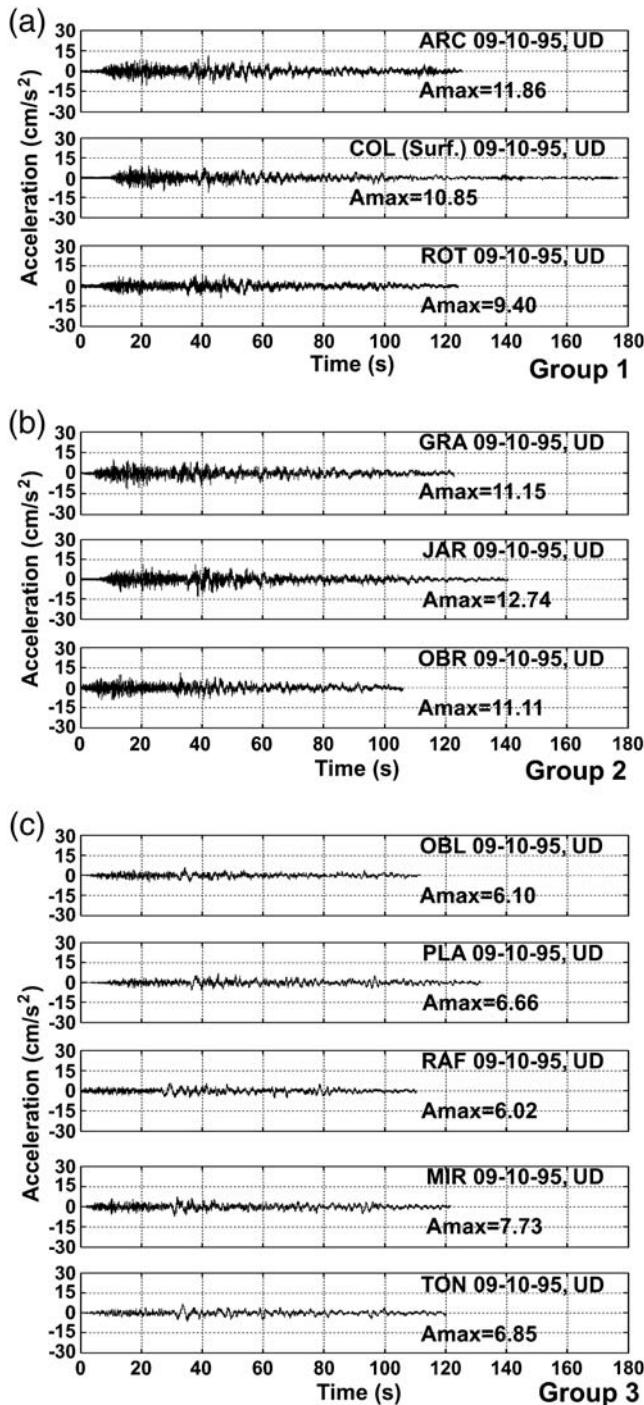

Figure 8. Accelerograms observed in the north–south (N–S) direction at Guadalajara's accelerographic network (Figs. 2, 5) for the M_w 8 CJ1995 earthquake for stations groups (a) 1, (b) 2, and (c) 3.

directly from each of the filtered recordings are included, and their values are shown in Figure 10 and Table 2. In both of them, the largest PGAs are those of station groups 1 and 2 (deployed on sites with $h > 20$ m); and, specifically at ARC and JAR, they were of ~24 cm/s², compared with PGA ~6 to ~8 cm/s² for station group 3 ($h \leq 20$ m). Figure 10 and Table 2 indicate that the PGAs for the UD components were

from ~9 to ~13 cm/s² for station groups 1 and 2 and ~7 cm/s² for station group 3.

In Table 2, the maximum recorded durations of the accelerograms of Figures 7–9 (i.e., the duration from the time each station accelerograph was triggered to when it was shut off during the CJ1995 earthquake) were observed at stations COL$_{surface}$ (which was interconnected to the station's

Figure 9. Accelerograms observed in the vertical (UD) direction at Guadalajara's accelerographic network (Figs. 2, 5) for the M_w 8 CJ1995 earthquake for stations groups (a) 1, (b) 2, and (c) 3.
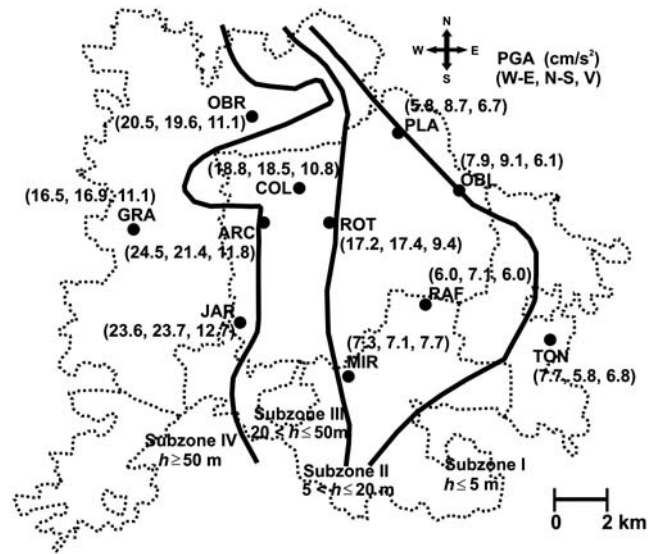

Figure 10. Peak ground acceleration (PGA) values (in cm/s^2) recorded in the west–east (W–E), north–south (N–S), and vertical (UD) directions by the 11 accelerographic stations of Guadalajara Accelerographic Networks during the M_w 8 CJ1995 earthquake.

downhole COL$_{rock}$ instrument, located at ~35 m depth; Fig. 4) and JAR (Figs. 2 and 5). Durations were ~160 and ~140 s, respectively. The average recording duration time for the three groups of stations was ~120 s.

　In Figures 11–13, the Fourier amplitude spectra of the accelerograms of Figures 7–9 are presented. In Figures 11 and 12, the shapes and the maximum values of the Fourier amplitude spectra for the W–E and N–S components of the three groups are, as a whole, similar for frequencies between ~0.05 and ~1 Hz; however, for frequencies between ~1 and ~3 Hz, those of groups 1 and 2 (with $h > 20$ m) present larger Fourier amplitudes, that is, from ~10 to ~40 cm/s compared with ~2 to ~20 cm/s for station group 3 (with $h \leq 20$ m). Also in Figures 11 and 12, the decrease of their Fourier amplitudes start at ~4, ~5, and ~0.9 Hz for station groups 1, 2, and 3, respectively.

　With respect to the Fourier amplitude spectra of the vertical components of the three groups of accelerograms, Figure 13 illustrates that for groups 1 and 2, for frequencies between ~0.05 and ~0.5 Hz, their shapes and their maximum amplitudes (of up to ~26 cm/s) are very similar; then, from ~0.5 Hz up to ~5 Hz, they show a plateau with a maximum amplitude of ~7 cm/s (except station GRA, which has a maximum amplitude of ~12 cm/s). From this frequency onward, the maximum amplitudes decrease. For station group 3, their amplitudes are very similar for the whole range of studied frequencies, their maximum amplitudes are ~18 cm/s up to 0.5 Hz, and the amplitudes decrease from 0.5 Hz onward.

Time and Frequency Domain Characteristics of the Recordings at COL$_{surface}$, COL$_{rock}$, and JAR Stations of Guadalajara for the M_w 8 CJ1995, and Its Larger M_w 5.75 Foreshock and M_w 5.92 Aftershock

　The W–E, N–S, and UD accelerograms and their Fourier amplitude spectra records at COL$_{surface}$ and COL$_{rock}$ stations (Fig. 2) for the CJ1995 earthquake are shown in Figures 14 and 15, respectively. In Figure 14a–c, the PGAs of the surface recordings are ~18 and ~11 cm/s^2, for the W–E, N–S, and UD components, respectively, and the PGAs of the

Table 2
Peak Ground Accelerations (PGA) and Durations (T_d) of the
Recordings at the 11 Guadalajara Accelerographic Stations
for the CJ1995 Earthquake

Station Group	Stations	PGA (cm/s^2)			T_d (s)
		W–E	N–S	UD	
1 (20 < h ≤ 50 m)*	ARC	24.49	21.38	11.87	~120
	COL	18.59	18.55	10.87	~160
	ROT	17.22	17.40	9.40	~120
2 (h > 50 m)	GRA	16.54	16.89	11.16	~120
	JAR	23.56	23.66	12.74	~140
	OBR	20.53	19.56	11.11	~120
3 (h ≤ 20 m)	OBL	7.87	9.13	6.10	~120
	PLA	5.78	8.71	6.67	~120
	RAF	5.97	7.08	6.03	~120
	MIR	7.32	7.12	7.74	~120
	TON	7.74	5.78	6.88	~120

*Thickness h of Guadalajara's sandy soil layers to competent basaltic rock.

rock (downhole) horizontal and vertical components are ~7 and ~6 cm/s^2, respectively. Their durations were ~160 s.

In Figure 15a,b, the frequency content and amplitudes of the W–E and N–S surface and rock signals are very similar up to ~1 Hz, but for frequencies larger than this value, the amplitudes of the surface recordings are considerably higher than the rock ones. The surface signals reaching their maximum Fourier amplitudes of ~25 cm/s for frequencies between 2 and 3 Hz (versus ~3 cm/s for the rock ones) and at ~8 Hz, where the Fourier amplitude of the surface N–S component is ~5 cm/s and in rock is ~0.9 cm/s. For the vertical components, their Fourier amplitudes of the surface and rock recordings are the same (except from 0.01 to 0.05 Hz) up to ~2 Hz; from this frequency onward, the Fourier amplitudes of the surface record are about three times larger than the rock one.

The PGAs of the W–E, N–S, and UD recordings for accelerograms at COL$_{surface}$ for event 1 (Table 1) are ~2, ~3, and ~2 cm/s^2, respectively, versus ~1, ~1, and ~0.6 cm/s^2 for the COL$_{rock}$ recordings, and their durations were ~80 s (Ⓔ Fig. S1, available in the electronic supplement to this article). The corresponding PGAs for the W–E, N–S, and UD recordings for event 3 (Table 1) are all ~2 cm/s^2, versus ~0.8, ~0.7, and ~0.6 cm/s^2 for the COL$_{rock}$ recordings, and their durations were ~60 s (Ⓔ Fig. S2).

In each of the accelerograms in Ⓔ Figures S1 and S2, there are two 10 s time windows, identified by signal and noise, that were used to perform a signal-to-noise frequency analysis of those recordings. The results of those analyses are shown in Figures S3–S14. The time windows and their corresponding Fourier amplitude spectra (H) are shown in parts (a) and (b), respectively, of Figures S3–S14; and the ratios of the H$_{signal}$/H$_{noise}$ are shown in part (c) of Figures S3–S14. From those figures, we concluded that the signal-to-noise ratios were satisfactory (H$_{signal}$/H$_{noise}$ ≥ 2, in which H is the Fourier amplitude spectra) for most of the frequency band of interest in this study.
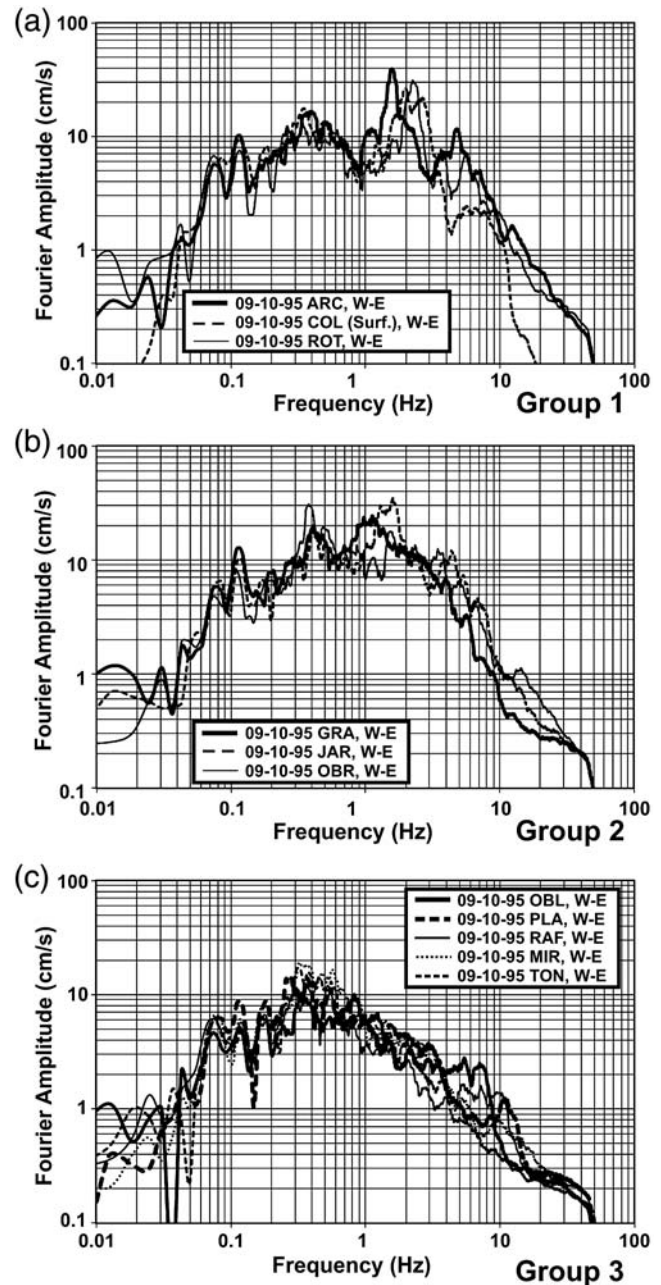

Figure 11. Fourier amplitude spectra of the accelerograms of Figure 7.

Ⓔ The Fourier amplitude spectra of the accelerograms of Figures S1 and S2 are presented in Figures S15 and S16, respectively. In these figures, the frequency content and amplitudes of the surface signals are higher than the corresponding signals in the rock recordings, especially for frequencies ≥1 Hz, reaching their maximum Fourier amplitudes for the same frequencies as those observed for the mainshock (Fig. 15).

From these observations, we can conclude that at station COL$_{surface}$, there is an amplification of the rock signals and an increase in their frequency content due to the propagation
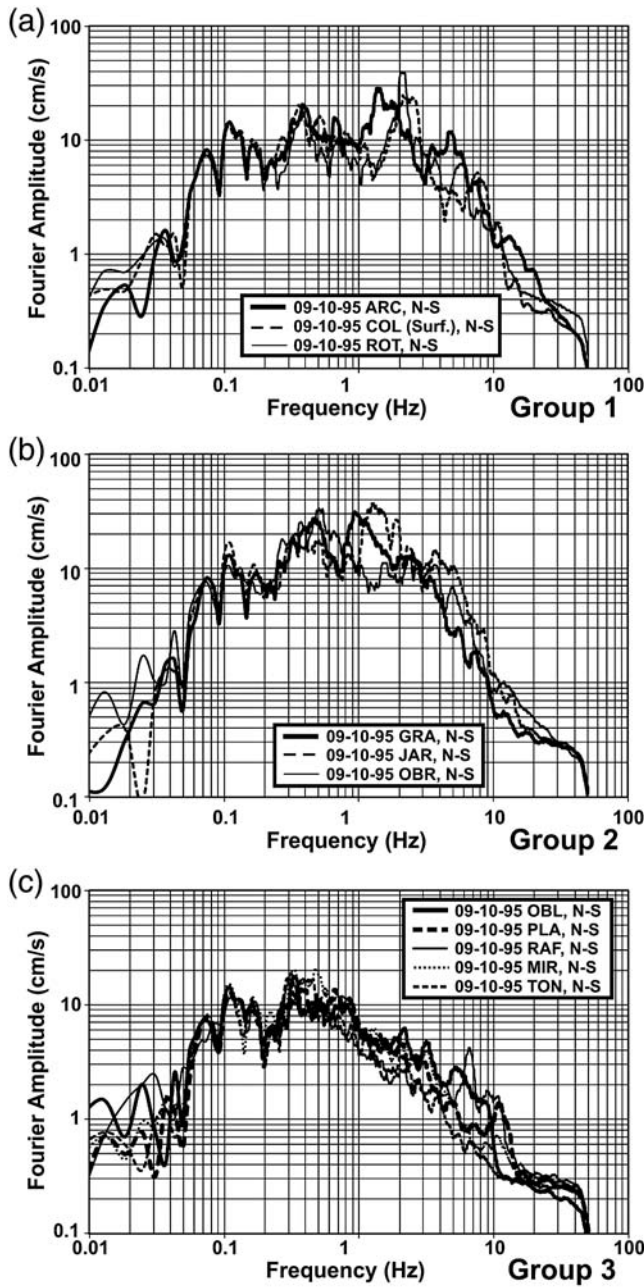
Figure 12.　Fourier amplitude spectra of the accelerograms of Figure 8.

Figure 13.　Fourier amplitude spectra of the accelerograms of Figure 9.

of signals in the 35 m layer of sandy soils of the COL station site (see Figs. 4 and 5).

The W–E, N–S, and UD components of the accelerograms recorded at station JAR (Fig. 2) for events 2 (mainshock) and 3 (largest aftershock) in Table 1 for the CJ1995 earthquake are shown in Ⓔ Figure S17a and S17b, respectively. For the horizontal and vertical components, the respective PGAs of the mainshock recordings are ~24 and ~13 cm/s^2; for the aftershock, they are ~3 and ~2 cm/s^2; and their respective durations are ~140 and ~30 s.

Ⓔ The Fourier amplitude spectra of the accelerograms of station JAR of Figure S17 are shown in Figure S18. In

Figure S18, the shapes and amplitudes of the spectra of the horizontal and vertical components are similar for frequencies less than ~0.9 Hz, but from 0.9 Hz to ~3 Hz, the amplitudes of the Fourier amplitudes of the horizontal recordings are up to 10 times greater than the corresponding amplitudes from the vertical recordings.

Local Site Effects of Guadalajara Superficial Soil Layers

In order to perform a detailed analysis of the potential local site effects at Guadalajara's 11 recording station sites
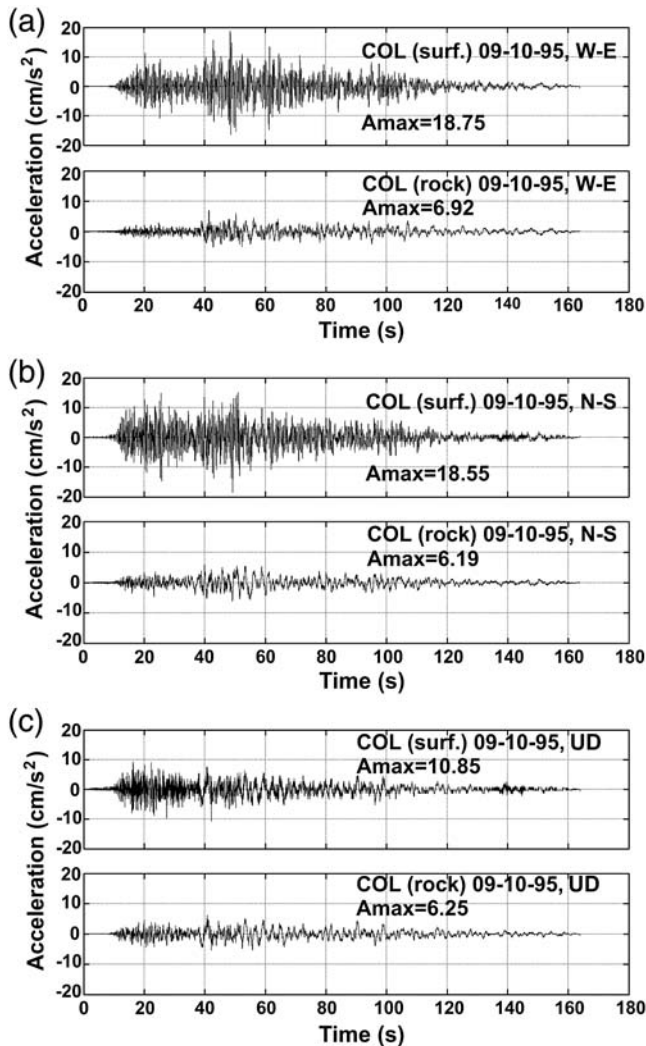
Figure 14.   Accelerograms observed at stations COL$_{surface}$ and COL$_{rock}$ for the M_w 8 CJ1995 earthquake in (a) west–east (W–E), (b) north–south (N–S), and (c) vertical (UD) directions. (Adapted from Chavez *et al.*, 2011.)

(Figs. 2 and 5), we applied the H$_{surface}$/V$_{surface}$ technique (in which H$_{surface}$ and V$_{surface}$ represent the respective Fourier amplitude spectra of the W–E and N–S and the UD records; Nakamura, 1989) to their recordings of the CJ1995 earthquake and obtained the transfer functions of 10 of the station recordings with respect to the rock site station TON recordings (i.e., the H$_i$/H$_{TON}$ and V$_i$/V$_{TON}$, in which i refers to stations 1–10).

For the recordings of events 1–3 (Table 1) from COL$_{surface}$ station, we calculated the H$_{surface}$/H$_{rock}$ and V$_{surface}$/V$_{rock}$ ratios (in which H$_{rock}$ represents the Fourier amplitude spectra of the W–E and N–S and V$_{rock}$ represents the vertical components of COL$_{rock}$ station). To compute the H and V values of the COL stations, or of the other 10 accelerographic stations of Guadalajara (Fig. 2), all of the durations of the accelerograms were used. We first will address the results obtained for stations COL and JAR and then the results corresponding to the three groups of recording station sites (Figs. 2 and 5, Table 2)
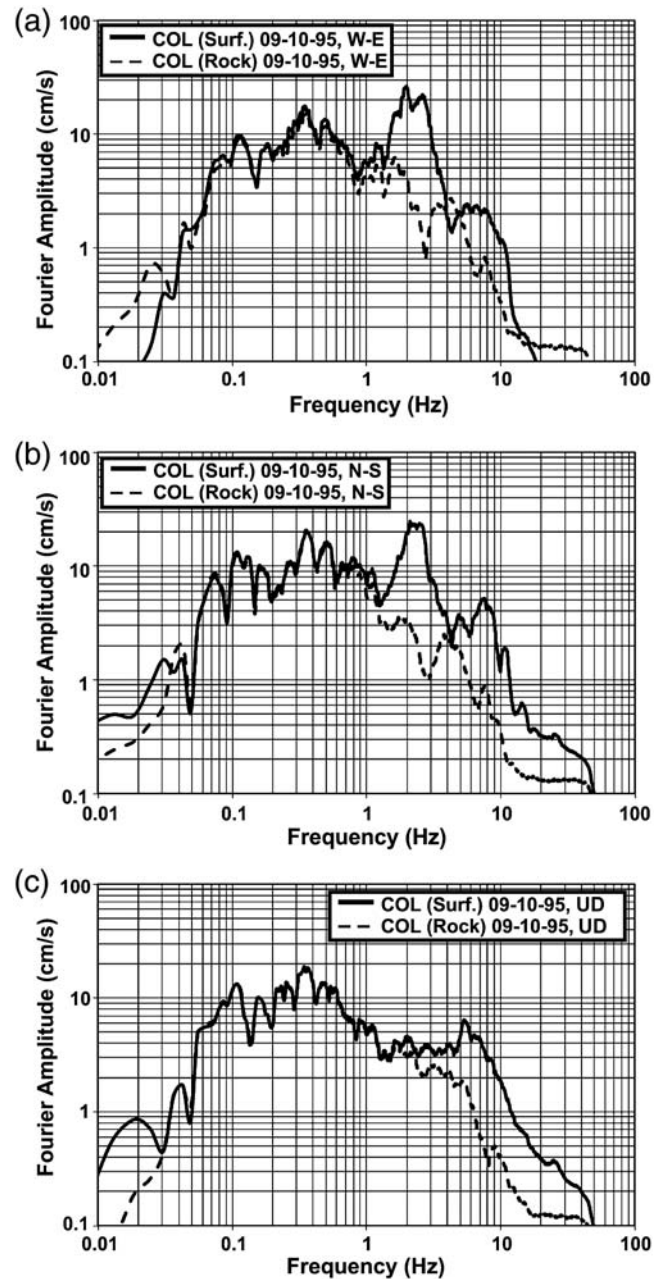
Figure 15.   Fourier amplitude spectra of the accelerograms shown in Figure 14.

Site Effects at Stations COL and JAR of Guadalajara Accelerographic Network

The results of the H$_{surface}$/V$_{surface}$ (Nakamura, 1989) and the H$_{surface}$/H$_{rock}$ ratios of the recordings at COL of the CJ1995 earthquake (events 1–3 in Table 1) are shown in Figure 16. The results of the former techniques and of the transfer functions of the W–E and N–S recordings of event 2 in Table 1 (the mainshock) are shown in Figure 16a,b. The H$_{surface}$/V$_{surface}$ and H$_{surface}$/H$_{rock}$ ratios are similar in their shape for the ∼0.05 to ∼50 Hz frequency band; however, for the frequency ∼2.65 Hz (the fundamental frequency of the soil layers at
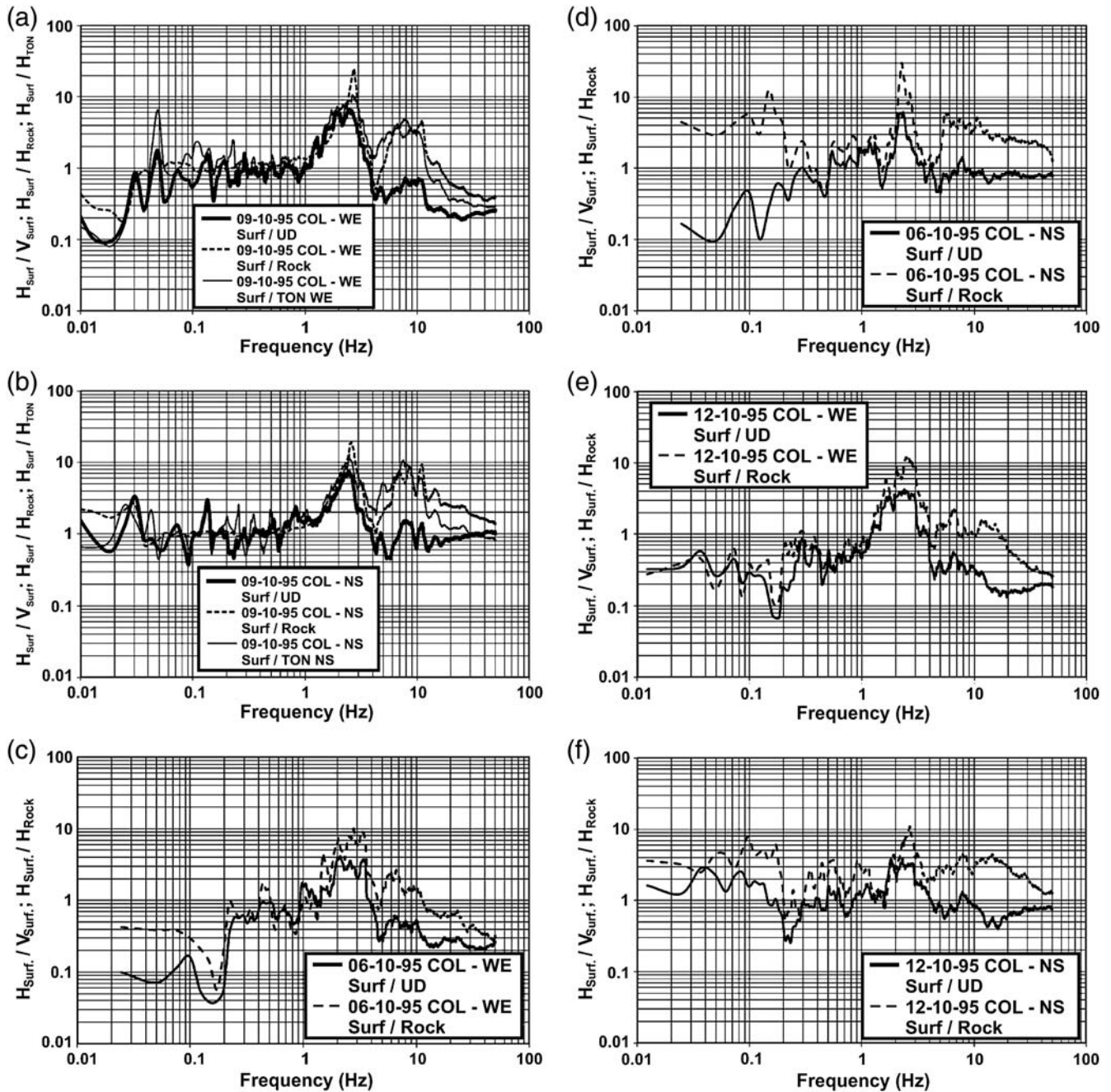
Figure 16. H/V and H_{surf}/H_{rock} ratios of the Fourier amplitude spectra for the accelerograms observed in the W–E and N–S directions at station $COL_{surface}$ of Guadalajara's accelerographic network (Figs. 2, 5) for (a, b) the 9 October M_w 8 CJ1995 earthquake, (c, d) the 6 October 1995 M_w 5.75 foreshock, and (e, f) the 12 October 1995 M_w 5.92 aftershock.

station $COL_{surface}$), the maximum amplitude of ~7 computed with the $H_{surface}/V_{surface}$ ratio underestimated the amplifications computed with the $H_{surface}/H_{rock}$ ratio by a factor of ~3. This observation is also valid for the 4–30 Hz frequency band; however, in this case, the underestimation factor is ~7 for the entire frequency band. A similar conclusion can be drawn from comparisons between the values of the transfer functions ($H_{COLsurface}/H_{TON}$) versus the ratio $H_{surface}/H_{rock}$ at a frequency of ~2.65 Hz: in this case, the underestimation factor is ~2 for the transfer function values, but the

$H_{surface}/H_{rock}$ ratio and the transfer functions ($H_{COLsurface}/H_{TON}$) values are almost the same for the ~6 to ~12 Hz frequency band.

The comparisons of the $H_{surface}/V_{surface}$ versus $H_{surface}/H_{rock}$ ratios for the recordings of the events 1 and 3 (Table 1) at station $COL_{surface}$ are shown in Figure 16c,d and 16e,f, respectively. From these figures, almost identical conclusions to those from the mainshock can be drawn, that is the $H_{surface}/V_{surface}$ ratios underestimate the $H_{surface}/H_{rock}$ ratios for the 2.65 Hz frequency by factors of ~2.5–5 and

underestimate for the ~4–30 Hz frequency band by a factor of up to ~4.

For station JAR, the results of the $H_{surface}/V_{surface}$ ratio (Nakamura, 1989) and the transfer functions (H_{JAR}/H_{TON}) technique applied to the W–E and N–S components of the recordings for event 2 (mainshock) and of the $H_{surface}/V_{surface}$ ratio for event 3 (aftershock) are shown in Ⓔ Figure S19a and 19b, respectively.

Ⓔ From Figure S19a, there are three conclusions: (1) the amplifications of the W–E and N–S recordings are similar in their shape for the ~0.05 to ~50 Hz frequency band; (2) the $H_{surface}/V_{surface}$ ratio values are ~0.5 than those of the transfer functions, which show a maximum amplification of ~12 in the ~1.2 to ~1.7 Hz frequency band; and (3) for the ~2.1 to ~20 Hz frequency band, the $H_{surface}/V_{surface}$ ratios and the transfer functions, follow a similar pattern to the one discussed for station $COL_{surface}$, with maximum values of ~3 and ~14 times at ~4.75 Hz, respectively. The results of the $H_{surface}/V_{surface}$ for JAR ratios (Ⓔ Fig. S19b) for the W–E and N–S records, for the largest aftershock of the CJ1995 earthquake are similar to the ones already discussed for the mainshock, confirming the amplification of the horizontal components at ~1.7 Hz for the CJ1995 events.

Site Effects at the 11 Recording Stations of Guadalajara Accelerographic Network

In order to analyze the local site effects at the three groups of Guadalajara recording station sites included in Table 2 for the CJ1995 earthquake, the Nakamura (1989) $H_{surface}/V_{surface}$ ratios and the transfer functions H_i/H_{TON} and V_i/V_{TON} (*i* is any of the other 10 recording stations, TON is TON station) were obtained for their W–E, N–S, and UD components. The results for the $H_{surface}/V_{surface}$ ratios are shown in Figures 17 and 18, and results for the transfer functions are shown for the directional components in Figures 19, 20, and 21, respectively.

In Figures 17 and 18, the values of the $H_{surface}/V_{surface}$ ratio for the W–E and N–S directions of group 1 are important (>2) for frequencies between ~1 and ~4 Hz, with maximum values ~8 (ARC), ~14 (ROT), and ~8 ($COL_{surface}$) at ~1.6, ~2.1, and ~2.7 Hz, (the fundamental frequencies of their soil layers), respectively. The $H_{surface}/V_{surface}$ amplification ratio values for group 2 are important (>2) for frequencies between ~0.4 and ~5 Hz, with maximum values of ~7 to ~9 (GRA), ~5 to ~6 (JAR), and ~4 to ~5.5 (OBR), at frequency ranges of ~0.8 to ~2.0 Hz (GRA), ~1.3 to ~1.7 Hz (JAR), and at ~0.52 Hz and from ~1.6 to ~3.5 Hz (OBR). Finally, the $H_{surface}/V_{surface}$ ratios of group 3 are important (>2) from ~5 to ~14 Hz and have maximum values of ~4.5 (OBL), ~6.1 (RAF), and ~4 (PLA) at ~7, ~6.5, and ~11 Hz, respectively; the maximum values for MIR and TON are under 2. For frequencies from ~4 to 50 Hz, the $H_{surface}/V_{surface}$ ratios are up to ~0.3, that is, implying a deamplification of the W–E and N–S recordings for stations $COL_{surface}$, GRA, and JAR.
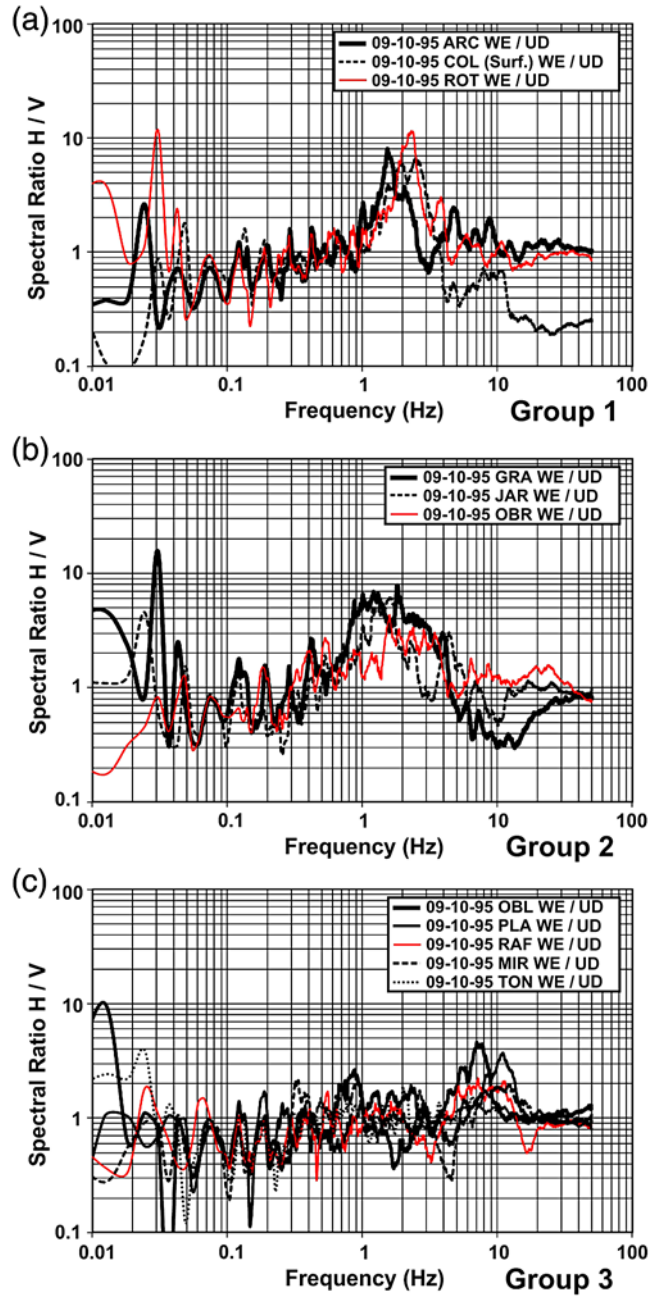

Figure 17. H/V ratios of the Fourier amplitude spectra for the accelerograms observed in the W–E direction at the stations of Guadalajara's accelerographic network (Figs. 2, 5) for the M_w 8 CJ1995 earthquake for groups (a) 1, (b) 2, and (c) 3. The color version of this figure is available only in the electronic edition.

Figures 19, 20, and 21 show the results of the transfer functions H_i/H_{TON} and V_i/V_{TON} for the three groups of stations. The transfer functions' shapes and amplitudes in Figures 19a,b and 20a,b are similar (but with higher amplitude values) to the H/V results of Figures 17a,b and 18a,b for frequencies less than ~3 Hz, respectively. However, for frequencies between ~3.5 and ~7.5 Hz, the transfer functions' figures show maximum values up to ~14, as large as the ones observed for frequencies less than ~3 Hz; these
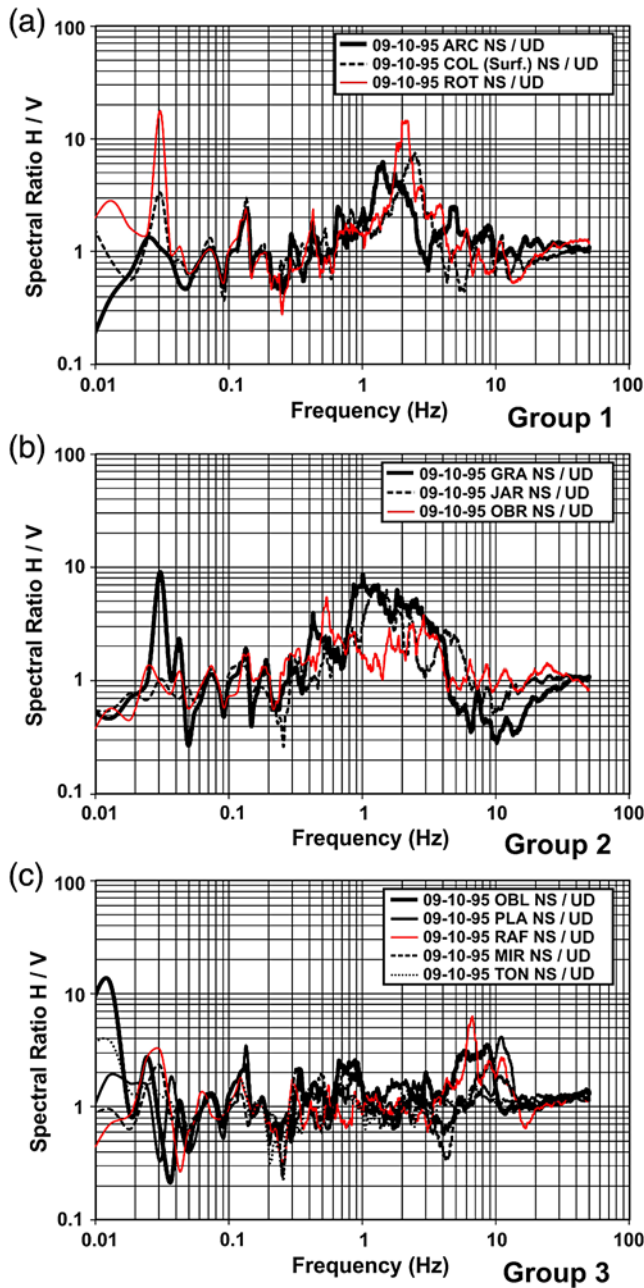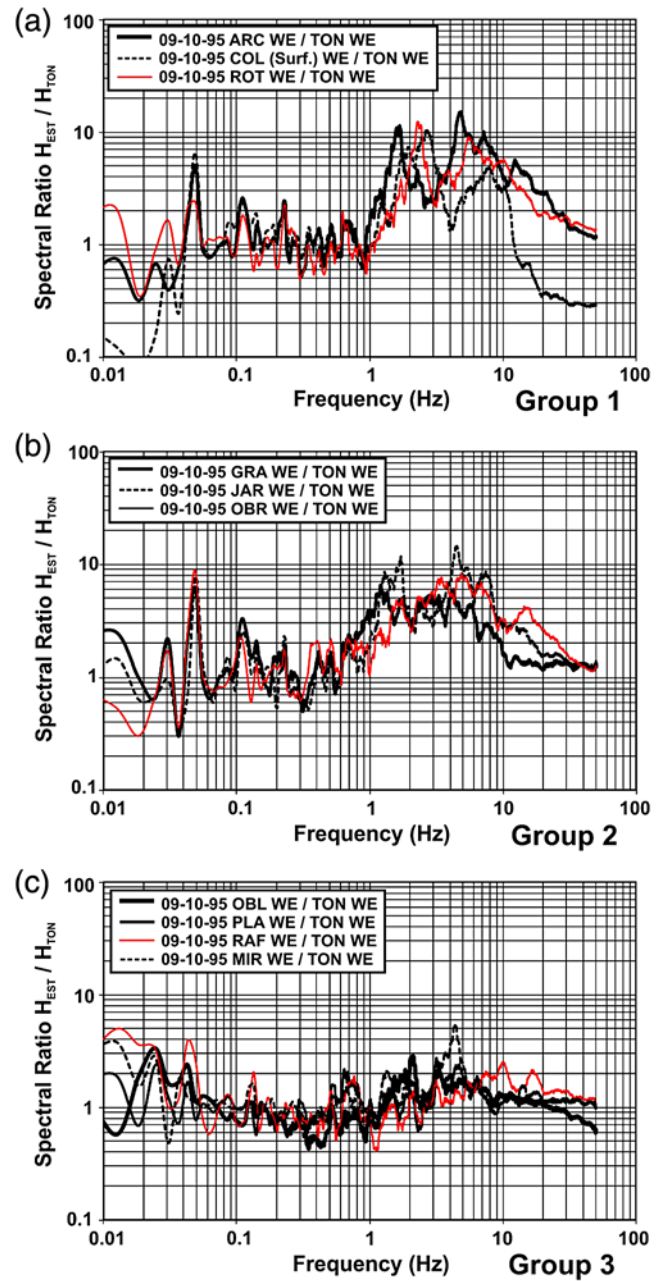
Figure 18. H/V ratios of the Fourier amplitude spectra for the accelerograms observed in the N–S direction at the stations of Guadalajara's accelerographic network (Figs. 2, 5) for the M_w 8 CJ1995 earthquake for groups (a) 1, (b) 2, and (c) 3. The color version of this figure is available only in the electronic edition.

Figure 19. H_i/H_{TON} ratios of the Fourier amplitude spectra for the accelerograms observed in the W–E direction at the stations of Guadalajara's accelerographic network (Figs. 2, 5) for the M_w 8 CJ1995 earthquake for groups (a) 1, (b) 2, and (c) 3. The color version of this figure is available only in the electronic edition.

amplitudes are grossly underestimated by the $H_{surface}/V_{surface}$ ratios, as was already mentioned for station $COL_{surface}$ (see Fig. 16a,b). From Figures 19c and 20c, it can be concluded that the transfer functions shapes and amplitudes for stations group 3 are also similar (but with higher amplitude values) to the H/V results of Figures 17c and 18c, respectively.

The shapes and amplitudes of the transfer functions for the vertical components (Fig. 21) are similar for station

groups 1 and 2, with maximum values up to ∼10 for frequencies between ∼5 and ∼8 Hz. For station group 3, the transfer functions show amplitudes between ∼2 and ∼5 for frequencies between ∼0.5 and ∼15 Hz.

We think the $H_{surface}/V_{surface}$ and H_i/H_{TON} values for frequencies less than ∼0.05 Hz (Figs. 17–21), which present maximum values of ∼10 (as large as those for frequencies greater than ∼1 Hz) for frequencies of 0.01, 0.03, and 0.05 Hz, are probably associated with low instrumental
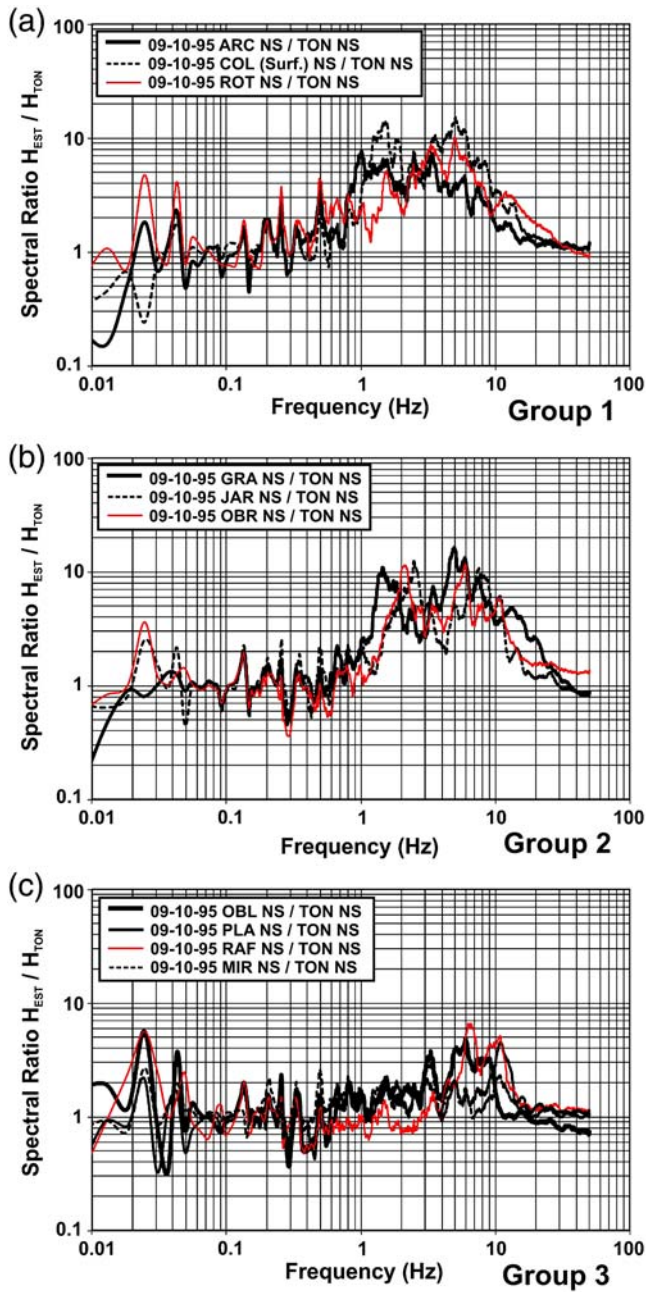
Figure 20. H_i/H_{TON} ratios of the Fourier amplitude spectra for the accelerograms observed in the N–S direction at the stations of Guadalajara's accelerographic network (Figs. 2, 5) for the M_w 8 CJ1995 earthquake for groups (a) 1, (b) 2, and (c) 3. The color version of this figure is available only in the electronic edition.

Figure 21. V_i/V_{TON} ratios of the Fourier amplitude spectra for the accelerograms observed in the UD direction at the stations of Guadalajara's accelerographic network (Figs. 2, 5) for the M_w 8 CJ1995 earthquake for groups (a) 1, (b) 2, and (c) 3. The color version of this figure is available only in the electronic edition.

resolution for those frequencies and/or numerical noise processing artifacts for this frequency band and therefore will disregard those results for the time being.

From the results discussed above, we can conclude that there are important local soil effects in the W–E, N–S, and UD directions at Guadalajara recording stations of groups 1 and 2, associated with their $h > {\sim}20$ m sandy soil layers lying on basaltic rock, compared with the $h \leq {\sim}20$ m soil layers of station group 3, as discussed by Chavez (1995, 2000).
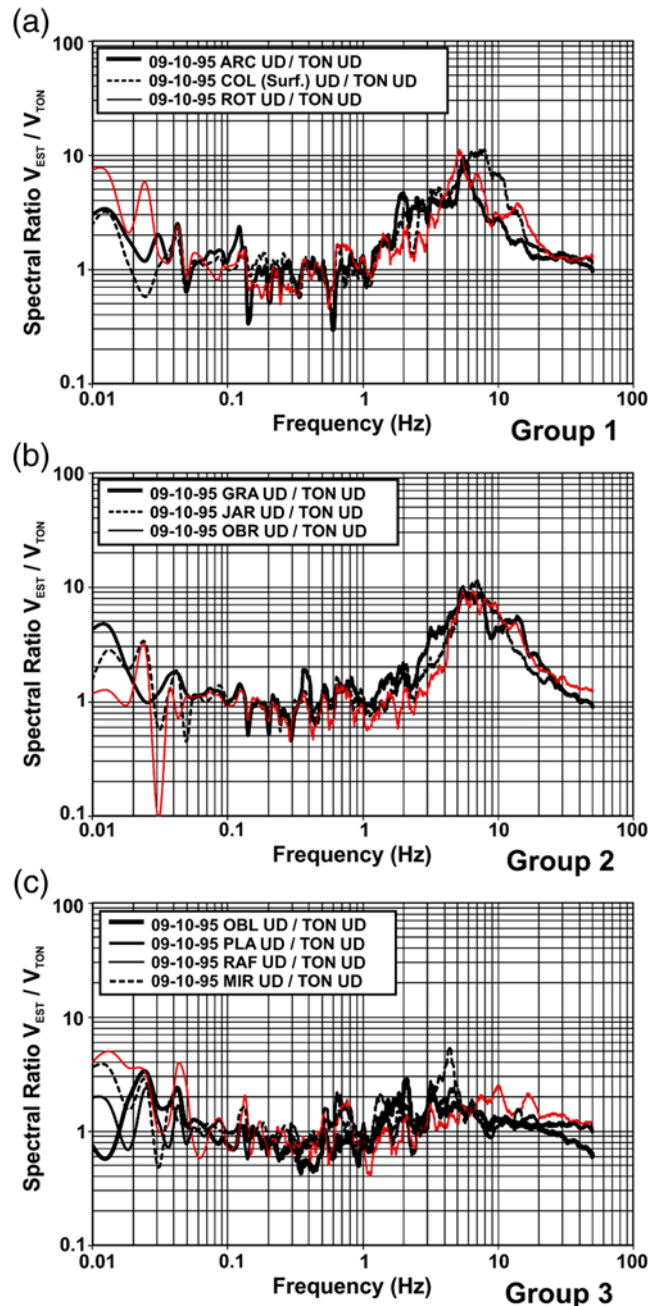
A Recurrent Neural Network to Estimate the Spatial Distribution of the Peak Ground Acceleration in Guadalajara for the 1995 M_w 8 Colima–Jalisco Earthquake

Among other strong ground motion intensity parameters used to display the seismic hazard at specific sites or urban areas, the PGA is widely used (García et al., 2007). For the CJ1995 M_w 8 earthquake, the PGA data available for

Guadalajara are the ones recorded at the 11 free-field accelerographic stations shown in Figure 10 and Table 2. In Figure 10, the distance among the recording stations varies from 2.5 to 8 km, and the city of Guadalajara is approximately 30 km long and 25 km wide.

Herewith, a new RNN procedure is proposed, validated, and applied to the mentioned PGA data to estimate its spatial distribution (x, y) in Guadalajara for the CJ1995 event based on the recorded PGA data shown in Figure 10.

Proposed Recurrent Neural Network Method

The RNN method proposed in this work, implicitly considers the influence of the spatial variability (x, y) of the soil properties in a surface of interest, in the estimation of its maximum seismic response (in this case PGA) to a particular earthquake, based on the recorded PGA at a finite number of sites. Herewith, the RNN method will be applied to Guadalajara surface, and the PGA recorded at its 11 accelerographic stations for the CJ1995 earthquake (Fig. 10).

The proposed 2D neural modeling uses the recorded PGA values at specific sites with coordinates $(x_i, y_i$, in which $i = 1, \ldots, M)$ for generating virtual PGA recordings at several nearby sites (at a spatial distance k of the recording sites), with coordinates $(x_j, y_j$, in which $j = 1 \ldots N)$ and (generally) $M \ll N$. Once the virtual recordings are obtained for the first time, the procedure is iteratively applied, assuming that the available recorded PGA for the actual iteration consists of the observed plus the virtual PGA values of the previous step. The iterations are performed until the PGA values are estimated for the N sites, covering the whole surface of interest, as shown schematically in Figure 22. The heuristic and theoretical bases of the proposed RNN method are presented next.

The proposed RNN procedure (synthesized in Fig. 22) is based on the first law of geography, "everything is related to everything else, but near things are more related than distant things" (Tobler, 1970). This conceptual observation is essentially connected with the spatial analysis. In spatial analysis, the concerns are in specific types of mathematical spaces (a mathematical space exists whenever a set of observations and quantitative measures of their attributes are available). In this case, we use a geographic space where the observations (in this case PGA) correspond to locations (sites A–D in Fig. 22a) in a spatial measurement framework that captures their proximity in the real world (Fig. 22a).

After defining the geographic space of interest (Fig. 22a) and tailoring Tobler's law to the problem of estimating the PGA values at the closest (located at k distances) points of the accelerographic recording stations (Fig. 22b), the virtual PGA recordings are estimated using the proposed RNN procedure. It is important to point out that the proposed RNN is not used here as a spatial interpolator for estimating the (PGA) variables at unobserved locations, the neural tool is a spatial regression method that captures spatial dependency in a kind of multidimensional regression analysis, providing information on spatial relationships among the variables involved.

The PGAs are estimated at the closest points where observations are available and are reused as training examples in the feature space (Fig. 22b); and, in a subsequent iteration, the most related PGA to these closest points (or virtual stations) are estimated (Fig. 22b). The new PGAs are introduced as patterns in the training set in an iterative procedure that stops when the neural estimations have covered the whole area (Fig. 22c–f).

The procedure shown schematically in Figure 22 is recurrent and transient in nature. Basically, it is a regression model with feedback capabilities that are achieved by connecting the neurons' outputs (PGA at unobserved locations) to their inputs. This is especially meaningful because the present output controls the output at the following instant. The virtual stations sample responses using monotonically increasing separation for the next situation. For solving this task, it is expected to operate a neural network (NN) capable of model dynamical functions, to store internal states, and to implement complex dynamics. To achieve this, the recurrent networks (also called associative memories or Hopfield memories networks; Hopfield, 1982) are used. In what follows, a brief discussion about this kind of NN is presented.

Recurrent Neural Network Architecture

The standard feedforward neural network, or multilayer perceptron (MLP), is the best-known member of the family of many types of neural networks (Haykin, 1999). Feedforward neural networks have been applied in tasks of prediction and classification of data for many years (Egmont-Petersen *et al.*, 2002; Theodoridis and Koutroumbas, 2008). Recently, a new class of neural networks, based on feedforward neural networks, was introduced. These dynamic neural networks, or neural networks for temporal processing, extend the feedforward networks with the capability of dynamic operation, which means that the neural network behavior depends not only on the current input (as in feedforward networks), but also on previous operations of the network.

Neural networks for temporal processing can be grouped into two classes. The first is called time-delay networks, and the second (used herein) consists of RNNs, which have recurrent connections, that is, networks in which the neuron outputs are fed back into the network as additional inputs (Graves *et al.*, 2009).

The fundamental feature of an RNN is that the network contains at least one feedback connection, so that activation can flow around in a loop. That enables the networks to perform temporal processing and learn sequences (e.g., perform sequence recognition/reproduction or temporal association/prediction). The architectures of RNN can take many different forms, but they all share two important common features:

1. They incorporate some form of MLP as a subsystem.
2. They exploit the powerful nonlinear mapping capabilities of the MLP plus some form of memory.
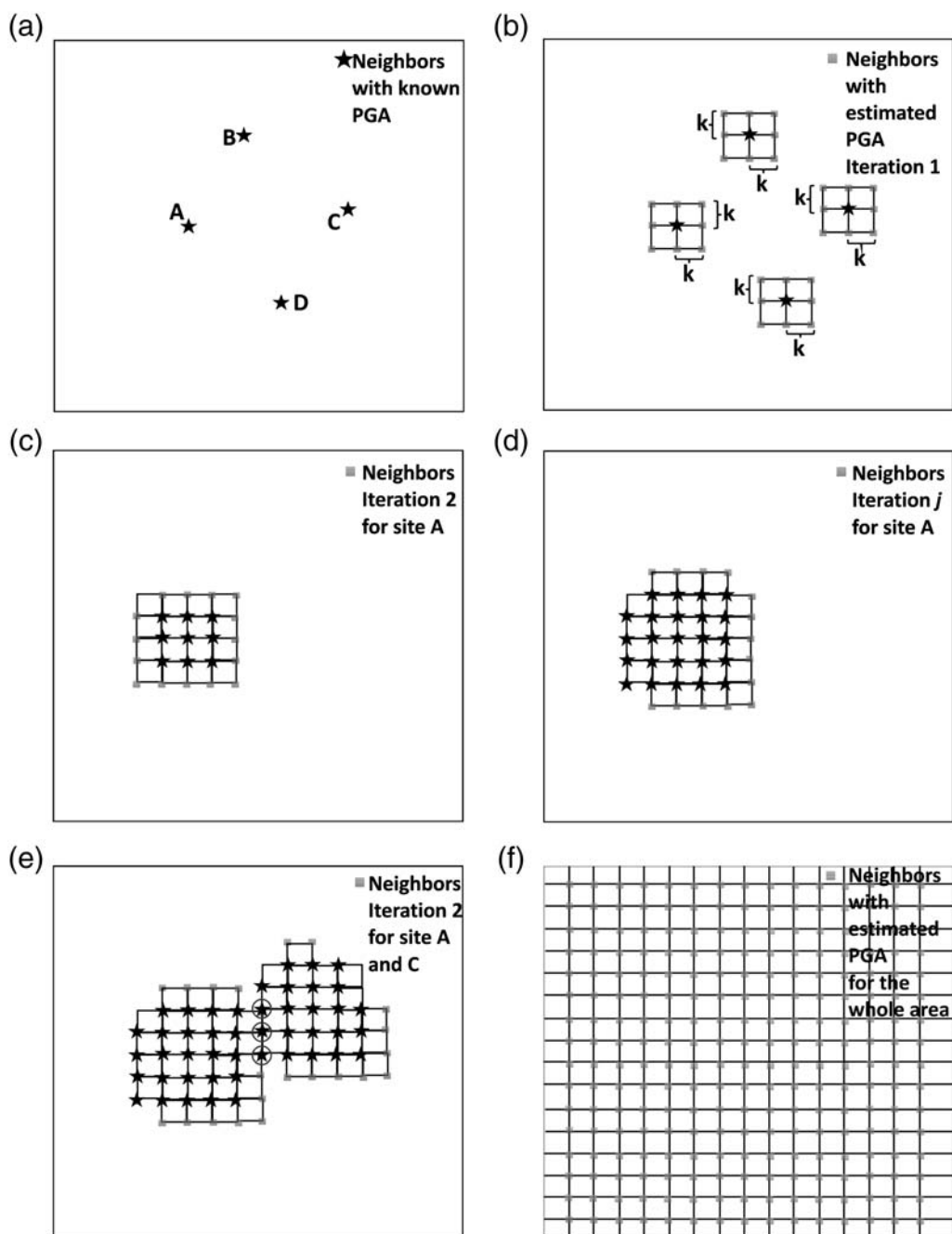
Figure 22.   Schematic representation of the proposed recurrent neural network (RNN) procedure. k is the distance to the stations where the PGAs are observed (identified by a star), and the squares represent the sites where the PGAs are estimated with the RNN procedure.

The learning capability of the NN network can be achieved by similar gradient descent procedures to those used to derive the backpropagation algorithm for feedforward networks (Hinton *et al.*, 2006).

Multilayer Networks.   Multilayer networks are static in nature (i.e., their output does not evolve with time, so for an input pattern there is an associated output), but they may acquire dynamic behavior (for an input pattern, the output has a transient state and converges to a value in the steady state), feeding back their inputs with previous settings of their outputs. The network consists of a static layer, which generally has a higher number of neurons with respect to the number of state variables of the system to identify, from which the output is directed to an adder, where it is subtracted from the previous value of the variable z_i, identified by the system, from this operation the derivative of each of the i state variables identified by the system is generated (see Fig. 23).

The dynamic recurrent multilayer network, the behavior of which is described in equation (1), can identify the behavior of an autonomous system ($u = 0$) (equation 2):
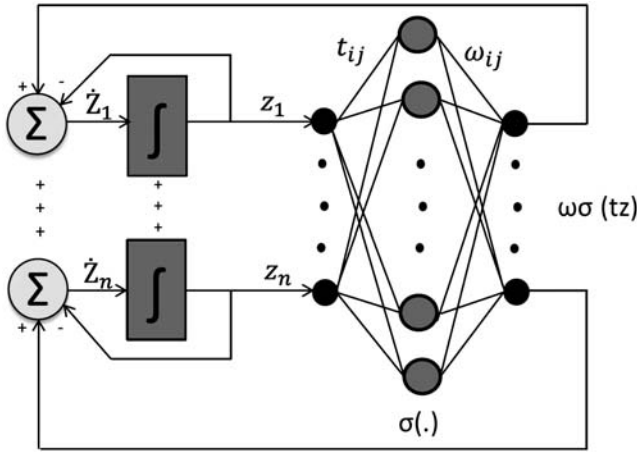
Figure 23. Dynamic multilayer networks, in which z_i is the output of the static layer i, $\dot{Z}_i$ is the derivative with respect to time of Z_i, t_{ij} is the expected value, ω_{ij} is the weight, and σ is the transfer function.
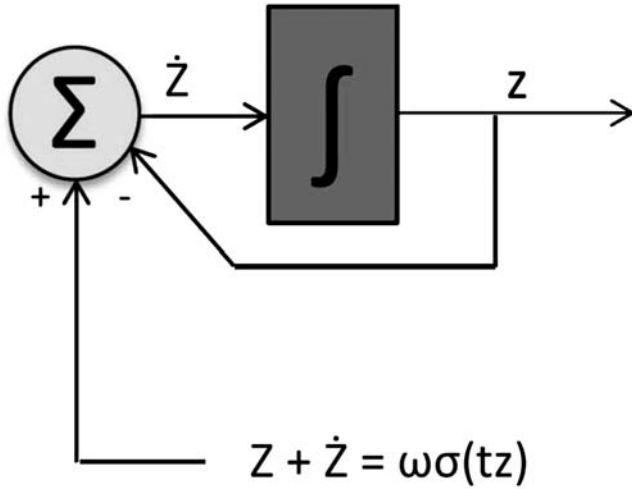

Figure 24. Training examples of the multilayer networks, in which Z is the output matrix of static layer, $\dot{Z}$ is the derivative with respect to the time of Z, ω is the weights matrix, t is the expected values matrix, and σ is the transfer function.

$$\frac{d}{dt}z = f(z) = Ax + \omega\sigma(\mathbf{T}z) \qquad (1)$$

and

$$\frac{d}{dt}x = f(x) = Ax + f_o(x), \qquad (2)$$

in which $z, x \in \mathcal{R}^n, f(z) : \mathcal{R}^n \to \mathcal{R}^n, A \in \mathcal{R}^{n \times n}, \omega \in \mathcal{R}^{n \times N}$, $f(x) : \mathcal{R}^n \to \mathcal{R}^n, \mathbf{T} \in \mathcal{R}^{n \times n}, \sigma(z) = [\sigma(z_1), \sigma(z_2), \dots \sigma(z_n)]$; z are the outputs of the multilayer system, $f(z)$ is the derivative of z, $f(x)$ is the derivative of x, A are the calculated values of the autonomous system, T the expected values of the dynamic neural network, $f_o(x)$ is the estimated $f(x)$, the transfer function $\sigma(\theta) = \text{tansig}(\theta)$, n is the number of state variables of the system, and N the number of neurons in the hidden layer. According to Haykin (1999), without loss of generality, if the source is assumed to be an equilibrium point, the system
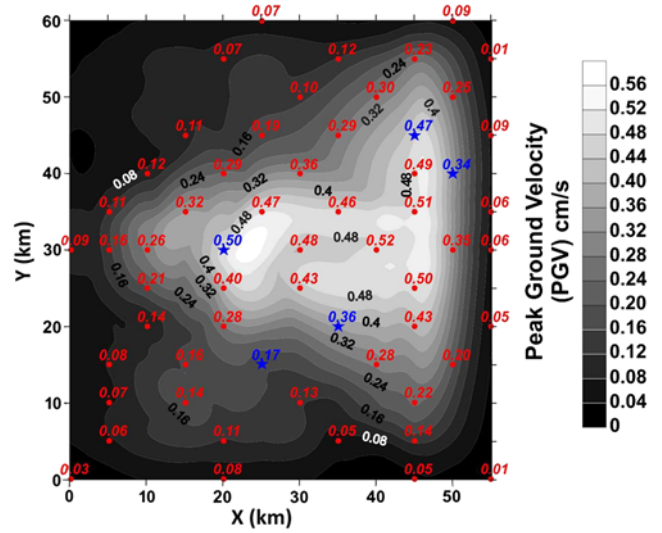

Figure 25. Synthetic peak ground velocity (PGV) pattern of the low-frequency wave propagation modeling of the 2004 M_w 6 Parkfield, California, earthquake. The pattern corresponds to 3300 cells (1 km² each) of the free surface of the physical domain of interest. The dots and the stars correspond to the coordinates (and respective PGV values) of the 59 cells selected for the test of the RNN proposed procedure. The distances among the 59 cells are from 5 to 15 km. The color version of this figure is available only in the electronic edition.

(equation 2) will be identified with the network (equation 1) about its attraction region and guarantees that the error in the approximation $e(t)$ is limited.

Learning Rules. The static stage of the dynamic recurrent multilayer network is usually trained with a backpropagation algorithm. These algorithms are widely described in the vast literature, for example in Hochreiter *et al.* (2001) and Serrano *et al.* (2009). The training patterns of the static layer of Figure 23 are different combinations of values of the state variables, and the target patterns are given by the sum of each state variable with their corresponding derivative, as shown in Figure 24. The network is trained after the structure of equation (3):

$$\frac{d}{dt}\begin{bmatrix} z_1 \\ z_2 \\ \vdots \\ z_n \end{bmatrix} = \begin{bmatrix} -z_1 \\ -z_2 \\ \vdots \\ -z_n \end{bmatrix} + \begin{bmatrix} W_{11} & W_{12} & \dots & W_{1n} \\ W_{21} & W_{22} & \dots & W_{2n} \\ W_{n1} & W_{n2} & \dots & W_{nn} \end{bmatrix}$$
$$\times \begin{bmatrix} \sigma(t_{11}z_1 + t_{12}z_2 + \dots + t_{1n}z_n) \\ \sigma(t_{21}z_2 + t_{22}z_2 + \dots + t_{2n}z_n) \\ \vdots \\ \sigma(t_{n1}z_1 + t_{n2}z_2 + \dots t_{nn}z_n) \end{bmatrix}, \qquad (3)$$

in which t_{ij} are the expected values of this variable. To ensure the network has identified the system dynamics, the Jacobian of the network at the source (equation 4) should have values very close to those of the system that has been approximated.
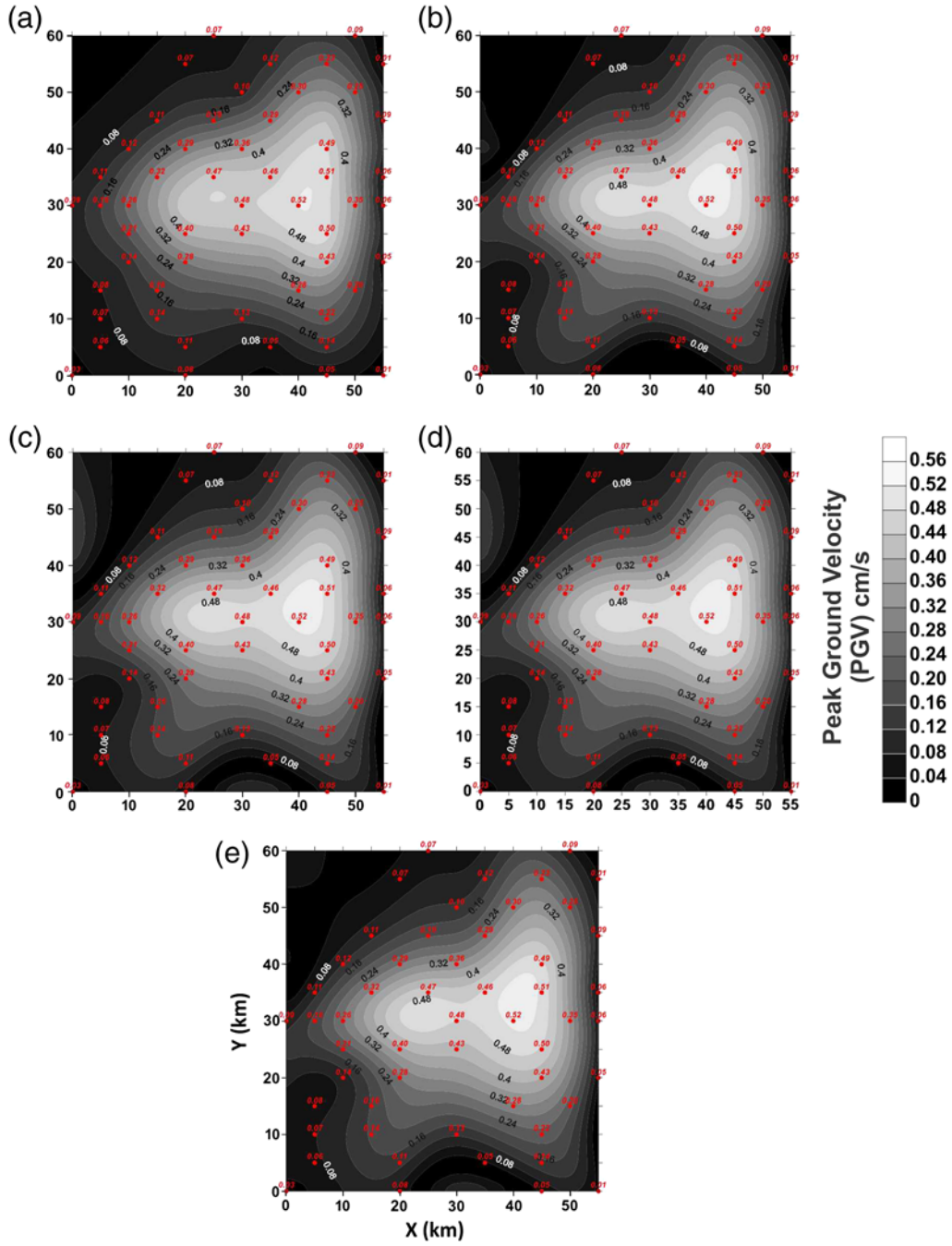
Figure 26. (a–e) Peak ground velocity (PGV) iteration patterns obtained by applying the RNN procedure (with $k = 1$ km; see Fig. 22) to the 54 cells identified by dots and the corresponding PGV values of Figure 25. (The PGV values of the five cells represented by stars were used to calibrate the RNN training results.) The color version of this figure is available only in the electronic edition.

$$J_M = -\mathbf{I}_n + \mathbf{WT}, \tag{4}$$

in which J_M is the Jacobian, $\mathbf{I}_n$ is the identity matrix of dimension n, $\mathbf{W}$ is the weights matrix, and $\mathbf{T} = \sigma(t_{ij}z_j)$. The dynamic multilayer network of Figure 23 can be transformed into a dynamic network (Hopfield type) by means of the following linear transformation:

$$\chi = \mathbf{T}z, \qquad \frac{d\chi}{dt} = \mathbf{T}\frac{dz}{dt}. \tag{5}$$

Generally the $\mathbf{T}$ matrix is square, but if it is not, the transformation is performed by means of the generalized inverse. The transformed network will have the structure

$$\frac{d}{dt}\chi = -\mathbf{I}_N\chi + \mathbf{TW}\sigma(\chi), \tag{6}$$

in which the new state vector $\chi \in \mathcal{R}^N$, $\mathbf{TW} \in \mathcal{R}^{N \times N}$, $\mathbf{I}_N$ is the identity matrix of dimension N, and the transformation (equation 5) extends the dynamic multilayer network (equation 3)
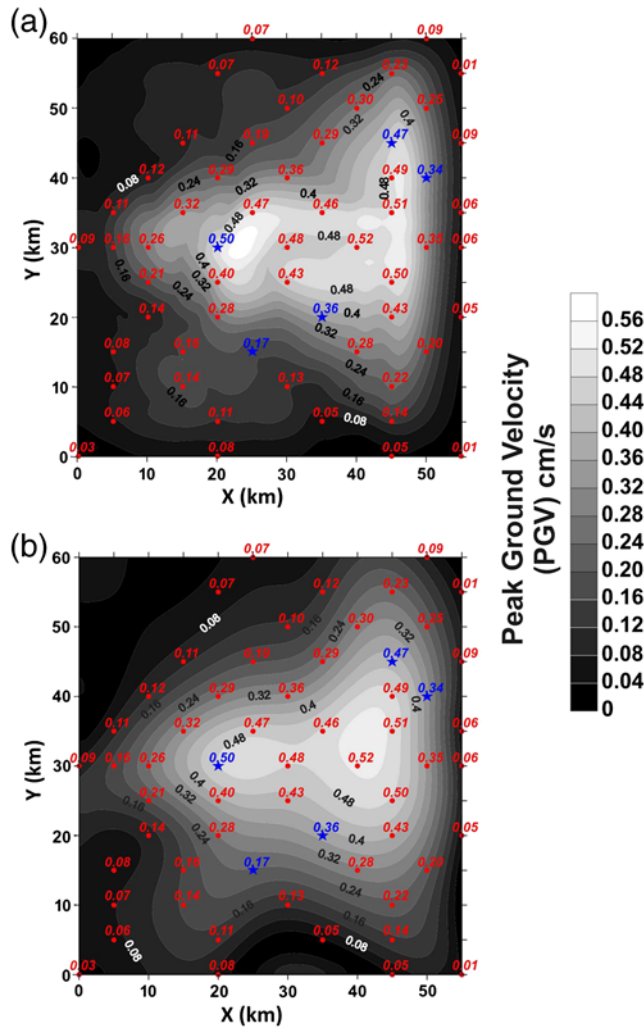
Figure 27. Comparison of (a) synthetic PGV patterns and (b) RNN PGV patterns of the M_w 6 Parkfield low-frequency wave propagation modeling (see Fig. 26 for the symbology). The color version of this figure is available only in the electronic edition.

into the dynamic recurrent Hopfield network (equation 6). In the Hopfield network, the number of states is greater than or equal to the number of states of the multilayer network $N \geq n$. After transformation, the network has the structure

$$\frac{d}{dt}\begin{bmatrix} \chi_1 \\ \chi_2 \\ \vdots \\ \chi_N \end{bmatrix} = \begin{bmatrix} -\chi_1 \\ -\chi_2 \\ \vdots \\ -\chi_N \end{bmatrix} + [\mathbf{TW}]\begin{bmatrix} \sigma(\chi_1) \\ \sigma(\chi_2) \\ \vdots \\ \sigma(\chi_N) \end{bmatrix}. \quad (7)$$

The Jacobian of the network described in equation (8) should have very close values to those of the system that has been approximated and should be equal to those of the multilayer network.

$$J_H = -\mathbf{I}_N + \mathbf{WT}, \quad (8)$$

in which J_H is the Hopfield Jacobian. An algorithm of the proposed RNN procedure, which includes the steps implicit in

equations (1)–(8), was developed in this work using tools of the Mathworks website (see Data and Resources). The validation of the algorithm is presented in the next section.

Validation of the Proposed Recurrent Neural Network Procedure

In order to validate the proposed RNN procedure, the 3D finite-difference wave propagation code applied by Chavez *et al.* (2010) to obtain the low-frequency synthetic 3D wave velocity propagation field of the M_w 7.9 Wenchuan earthquake was used to generate similar wave propagation fields, in this case the one associated with the 28 September 2004 M_w 6 Parkfield, California, earthquake (Custodio *et al.*, 2005). The proposed RNN procedure was applied then to a small, discrete sample of the punctual values of the synthetic velocity field in a given direction, to try to reproduce the pattern of the synthetic wavefield.

A physical domain of 100 (length in the *x* direction) × 80 (width in the *y* direction) × 60 (depth in the *z* direction) km^3, with the geological structure adopted by Custodio *et al.* (2005) for the region near the epicenter of the Parkfield earthquake, was used. The simulation used a seismic source geometry of 40 km length (in the *x* direction) × 14 km width, with a strike-slip mechanism, hypocenter at 8.1 km depth, a dip of 89°, and the average kinematic slip distribution and rise time of 0.3 s suggested by Custodio *et al.* (2005). A spatial discretization (in the *x*, *y*, and *z* directions) and a time step of 1 km and 0.03 s, respectively, were used in the simulation.

For the test of the RNN procedure, a subdomain of 55 (length, *x* direction) × 60 (width, *y* direction) km^2 of the free surface of the 100 (length in the *x* direction) × 80 (width in the *y* direction) km^2 physical domain (where the largest peak ground velocity [PGV] occurred) was selected. Therefore, the 3D synthetic seismograms corresponding to 3300 cells (55 × 60) of 1 km^2 each in the free surface of the discretized 3D volume were obtained. The 3300 PGVs in the *y* direction were retrieved from those synthetic seismograms. The resulting PGV wave velocity field in this direction is presented in Figure 25. The PGV values varied from 0.02 to 0.56 cm/s, which correspond to the edges and the central parts of the surface of 55 × 60 km^2 subdomain, respectively.

The validation test of the proposed RNN procedure consisted of trying to reproduce the PGV pattern of Figure 25, by applying the RNN algorithm to a very small fraction of the synthetic 3300 PGV available values. The test was conducted as follows: First, the coordinates and PGV values of 59 cells were selected (54 of them identified by dots, and 5 by stars in Fig. 25) out of the 3300 available. The distance among the centers of the 59 cells varied from 5 to 15 km (Fig. 25). Then, using a spatial distance $k = 1$ km (see Fig. 22), the RNN algorithm was applied to the 54 values to generate a PGV velocity field at 3300 cells, each one being 1 km^2.

The results of the computation are shown in Figure 26, in which the evolution of the pattern of the PGV velocity field

Synthetic and Neural Network Datasets

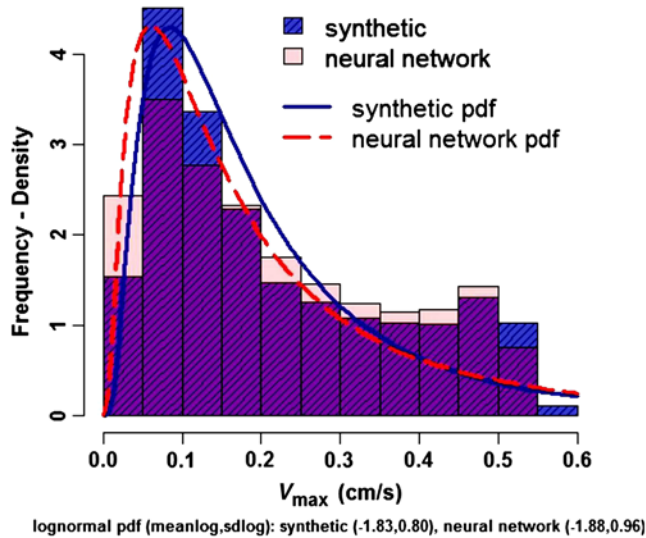lognormal pdf (meanlog,sdlog): synthetic (-1.83,0.80), neural network (-1.88,0.96)

Figure 28. Synthetic and RNN PGV histograms of the PGV values used to generate Figure 27 and their fitted lognormal probability density functions. The color version of this figure is available only in the electronic edition.

is exposed in the sequence of five critical iterations of the RNN procedure. It is important to mention that the five PGV values represented by the stars in Figures 25 and 26 were left out of the RNN calculations; they were used to calibrate the RNN training result, which was found satisfactory.

The comparison of the original 3D finite-difference synthetic PGV velocity field pattern with the one resulting with the RNN procedure is presented in Figure 27. The main features and values of the synthetic PGV field are preserved in the pattern obtained with the RNN procedure. The histograms and the fitted lognormal probabilities density functions corresponding to the 3300 PGV values of both the synthetic and RNN PGV results are shown in Figure 28. The main differences in the histograms and the corresponding fitted lognormal probability density functions are for PGVs ≤ 0.15 cm/s; for PGVs > 0.15 cm/s, they are very similar. A Kolmogorov–Smirnov test was carried out to compare both lognormal fitted distributions, and the results are shown in Table 3. For $n = 1000$ data points, the value distance of the Kolmogorov–Smirnov test is 0.064; and for $\alpha = 0.025$ (discussed in Table 3), the critical distance value is $0.066 > 0.062$, implying that the two lognormal distributions of Figure 28 can be considered (with a 97.5% confidence) to be statistically equal.

Estimation of the Spatial Distribution (x, y) of PGA in Guadalajara for the CJ1995 Earthquake by Applying the Proposed Recurrent Neural Network Method

Taking into account the results obtained in the validation of the proposed RNN procedure presented in the previous

Table 3
Critical values (CV) of the Kolmogorov–Smirnov
Test* for several α, for $n = 1000$ data points

α	CV
0.1	0.055
0.05	0.061
0.025	0.066
0.01	0.073
0.005	0.077
0.001	0.087

The value distance $D_{n,n}$ of the Kolmogorov–Smirnov test applied to the two fitted lognormal distributions of the PGV synthetic and the recurrent neural network for $n = 1000$ is 0.064.
*The null hypothesis of the two sample tests is the equality of the two empirical distributions. The distance between two empirical distribution functions $F_{1,n}$ and $F_{2,n}$, each with n data points, is defined as $D_{n,n} = \sup_x |F_{1,n}(x) - F_{2,n}(x)|$. The null hypothesis at the level α is rejected if the distance $D_{n,n}$ is higher than $c(\alpha) \times (2n/n^2)^{1/2}$, in which $c(\alpha)$ is the coefficient associated to a specific value of the significance level α, of the Kolmogorov–Smirnov test. For $n = 1000$ and $\alpha = 0.025$, the CV value is $0.066 > 0.064$, implying that the two lognormal distributions of Figure 28 can be considered to be statistically equal with a 97.5% confidence.

section, this methodology was applied using a spatial distance $k = 0.3$ km (see Fig. 22, compared with the distances > 2.8 km among the Guadalajara accelerographic recording stations shown in Fig. 2), first to the 10 PGA values in the W–E and then to the ones in the N–S directions that were included in Figure 10. (The PGA values of station ROT were not used in the calculations, but to verify the RNN training results.)

The results obtained with the application of the RNN's scheme (Fig. 22) to estimate the spatial distribution of PGA in Guadalajara for the CJ1995 earthquake are shown in Figures 29–32. In Figures 29 and 31a–f, the evolution of the RNN computations of the PGA patterns in the W–E and N–S directions are shown. The respective final PGA patterns are presented in Figures 30 and 32. These figures include the recorded PGA values at the 11 recording stations of Guadalajara (Fig. 10) and the RNN estimated patterns of PGAs for the W–E and N–S components, respectively.

The following conclusions can be drawn from Figures 30 and 32: (a) The estimated PGA values for the CJ1995 earthquake in Guadalajara varied from ~2 to ~27 cm/s². (b) Two PGA subzone values can be observed, one with PGA values ≤ 17 cm/s² and the second with PGAs > 17 cm/s². Those PGA subzone values, roughly correspond to the geotechnical subzones I–II and III–IV, proposed by Chavez (1995, 2000), U. Saborio and O. Saborio, for Guadalajara; the subzones with thicknesses of sandy soil layers to competent basaltic rock of $h \leq 20$ m and $h > 20$ m, respectively (see Fig. 2). (c) These results agreed with the findings about the site-effect amplifications of Guadalajara's sandy soils discussed previously, which showed important local amplification effects for station sites with $h > 20$ m soil layers, from the recordings in Guadalajara of the CJ1995 mainshock, foreshock, and aftershocks in its accelerographic network.
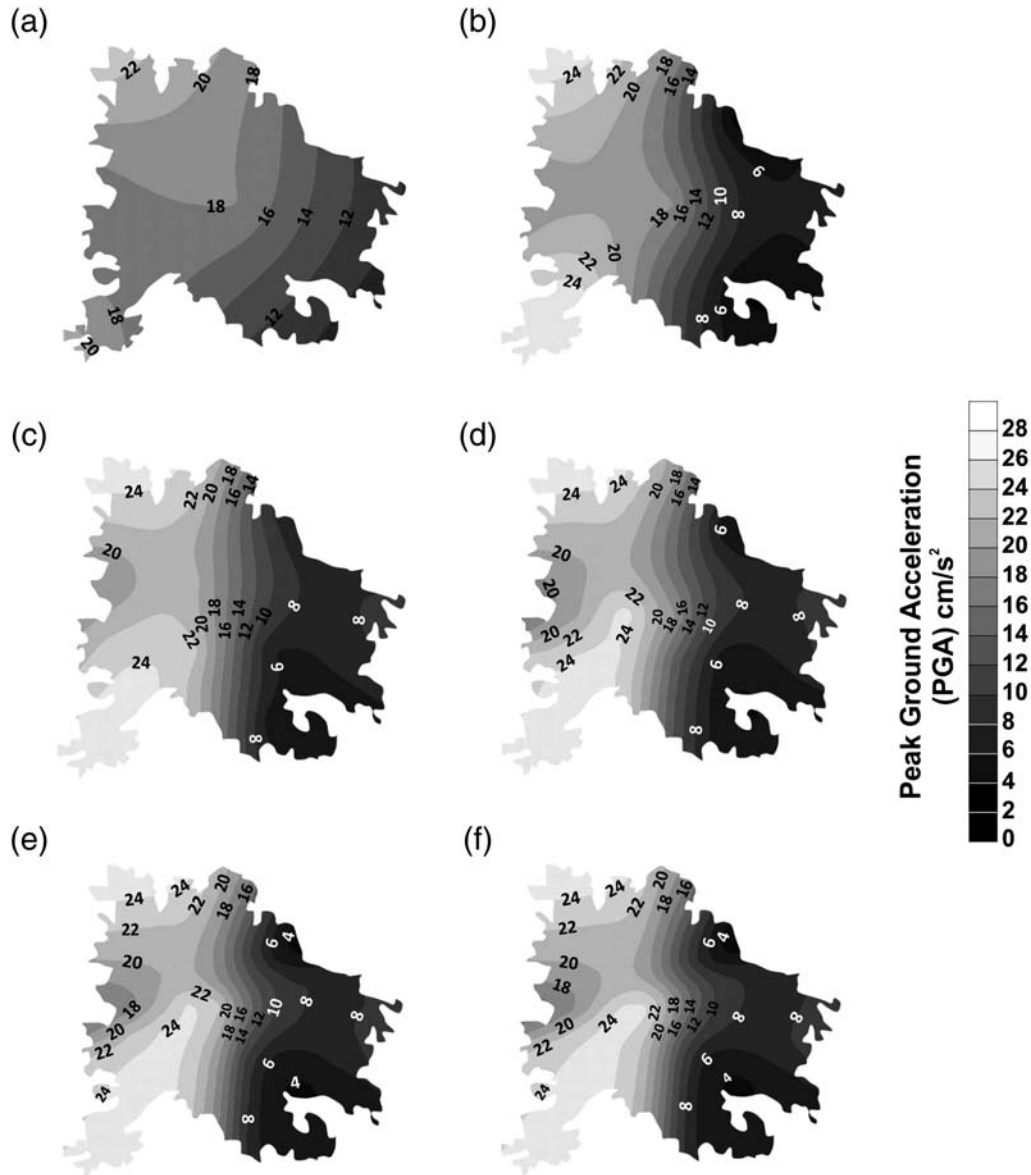
Figure 29. (a–f) Estimated PGA iterations patterns in the W–E direction obtained for Guadalajara for the M_w 8 CJ1995 earthquake by applying the proposed RNN procedure (with a distance $k = 0.3$ km; see Fig. 22) to the 10 recorded PGA values in the W–E direction, shown in Figure 10. (The PGA value of station ROT was used to verify the RNN training results.)

Discussion and Conclusions

1. Comparing the results obtained using (a) the $H_{surface}/V_{surface}$, (b) the transfer function $H_{surface}/H_{rock–reference}$, and (c) the $H_{surface}/H_{downhole–rock}$ criteria applied to the W–E, N–S, and UD records of the $COL_{surface}$ accelerographic station of Guadalajara for the CJ1995 earthquake, we concluded that for this station site, the (a) and (b) criteria underestimate the actual soil amplifications by ~4 to ~6 and by ~2, respectively when compared with results obtained using the (c) criterion (~20 times at ~2.7 Hz). However, for frequencies > 4 Hz, the (b) criterion gives similar amplification values (e.g., of up to ~10 at ~7.5 Hz) to those obtained using the (c) criterion, while the (a) criterion grossly underestimates and even indicates a deamplification of signals for frequencies > 4 Hz.

2. From the results obtained for the W–E, N–S, and UD records observed at the 11 free-field accelerographic stations of Guadalajara for the CJ1995 earthquake by applying the $H_{surface}/V_{surface}$ ratios and the transfer functions H_i/H_{TON} and V_i/V_{TON} (i is station 1–10, and TON is a rock site reference station), we concluded that local site effects were identified in all the station sites. Important local site effects exist at Guadalajara (amplifications of up to ~15 times, for frequencies between ~1 and ~3 Hz and between ~4 and ~7 Hz) for the station sites deployed on sandy soil layers with thicknesses $h > 20$ m to the basaltic rock, compared with the site effects at stations
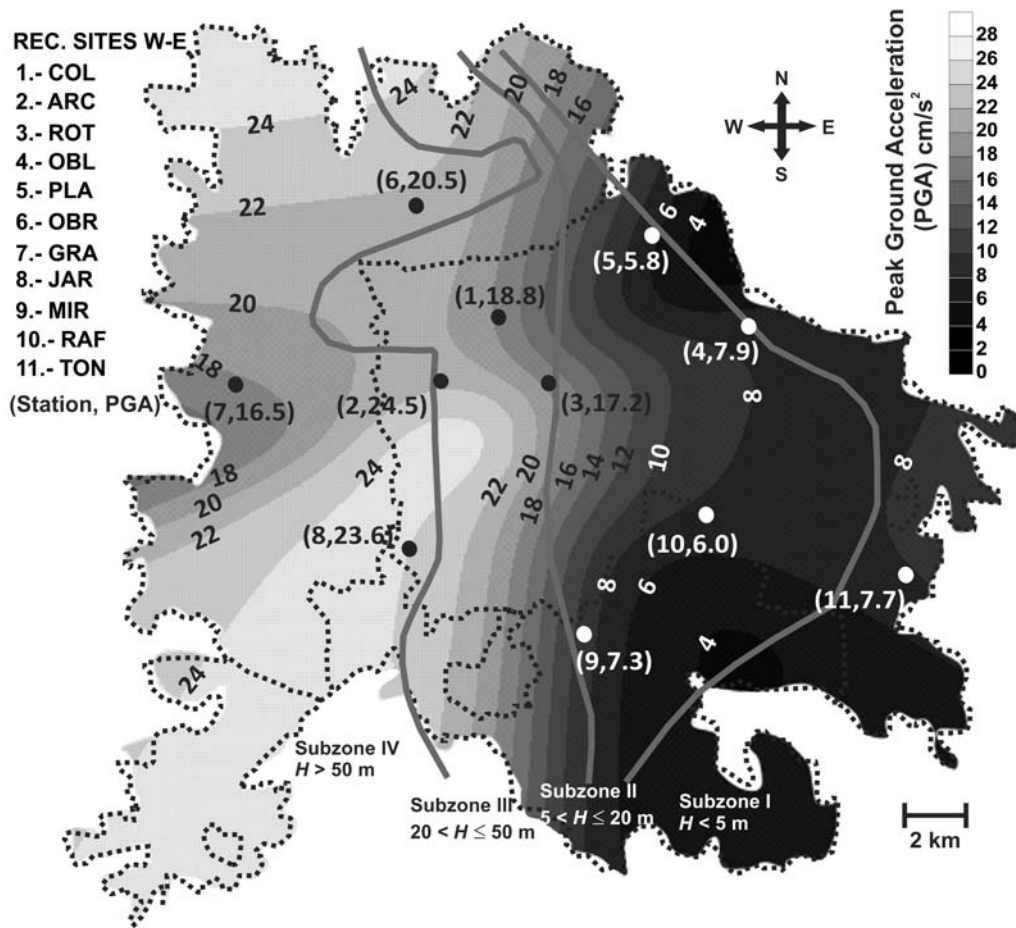
Figure 30. Estimated PGA pattern in the W–E direction for Guadalajara for the M_w 8 CJ1995 earthquake, obtained by applying the proposed RNN procedure (with a distance $k = 0.3$ km; see Fig. 22) to the 10 recorded PGA values, included beside the black and white dots identifying the recording stations. (The PGA value of station ROT was used to verify the RNN training results.)

sites with $h \leq 20$ m (amplifications of up to ~5 times, for frequencies between 4 to 10 Hz).

3. Based on the geotechnical characteristics of the superficial sandy layers of Guadalajara, we think the transfer function $H_i/H_{reference-rock-station}$ would provide a more reliable estimate of the site effects in Guadalajara than the $H_{surface}/V_{surface}$ technique, particularly for sites with $h > 20$ m, even though the $H_i/H_{reference-rock-station}$ underestimates the actual site-effect amplifications (e.g., by a factor of 2 at the $COL_{surface}$ station).

4. An RNN procedure was proposed, validated, and applied to estimate the spatial distribution (x, y) of the PGA in Guadalajara for the M_w 8 CJ1995 earthquake. The input information consisted of the location and the PGAs recorded for this event at Guadalajara's 11 accelerographic station sites.

5. The validation of the proposed RNN procedure was carried out for a low-frequency PGV synthetic field (in the y direction) of the 2004 M_w 6 Parkfield, California, earthquake, which was generated with the 3D finite-difference wave propagation code used to obtain the PGV fields for the M_w 7.9 Wenchuan earthquake (Chavez et al., 2010).

Among other results of the validation exercise, two are of special note. First, the main features and values of the synthetic PGV field are preserved with the proposed RNN procedure applied to only 54 PGV values (out of the 3300 synthetic values available). Second, from a Kolmogorov–Smirnov test carried out on the two lognormal distributions fitted to the histograms of the 3300 PGV values of the synthetics and of the obtained with the RNN procedure, the distributions can be considered to be statistically equal with a 97.5% confidence.

6. From the application of the proposed RNN procedure to the PGA values recorded in the W–E and N–S directions for the CJ1995 earthquake at the 11 accelerographic stations of Guadalajara (Figs. 30 and 32), we concluded the estimated PGA values in Guadalajara for this event varied from ~2 to ~27 cm/s^2.

7. Estimated values of two PGA subzones were found for Guadalajara, one with PGA values ≤ 17 cm/s^2 and the second with PGAs > 17 cm/s^2. Those PGA subzone values roughly correspond to the geotechnical subzones I–II and III–IV, proposed by Chavez (1995, 2000), U. Saborio and O. Saborio for Guadalajara, that is, the subzones with
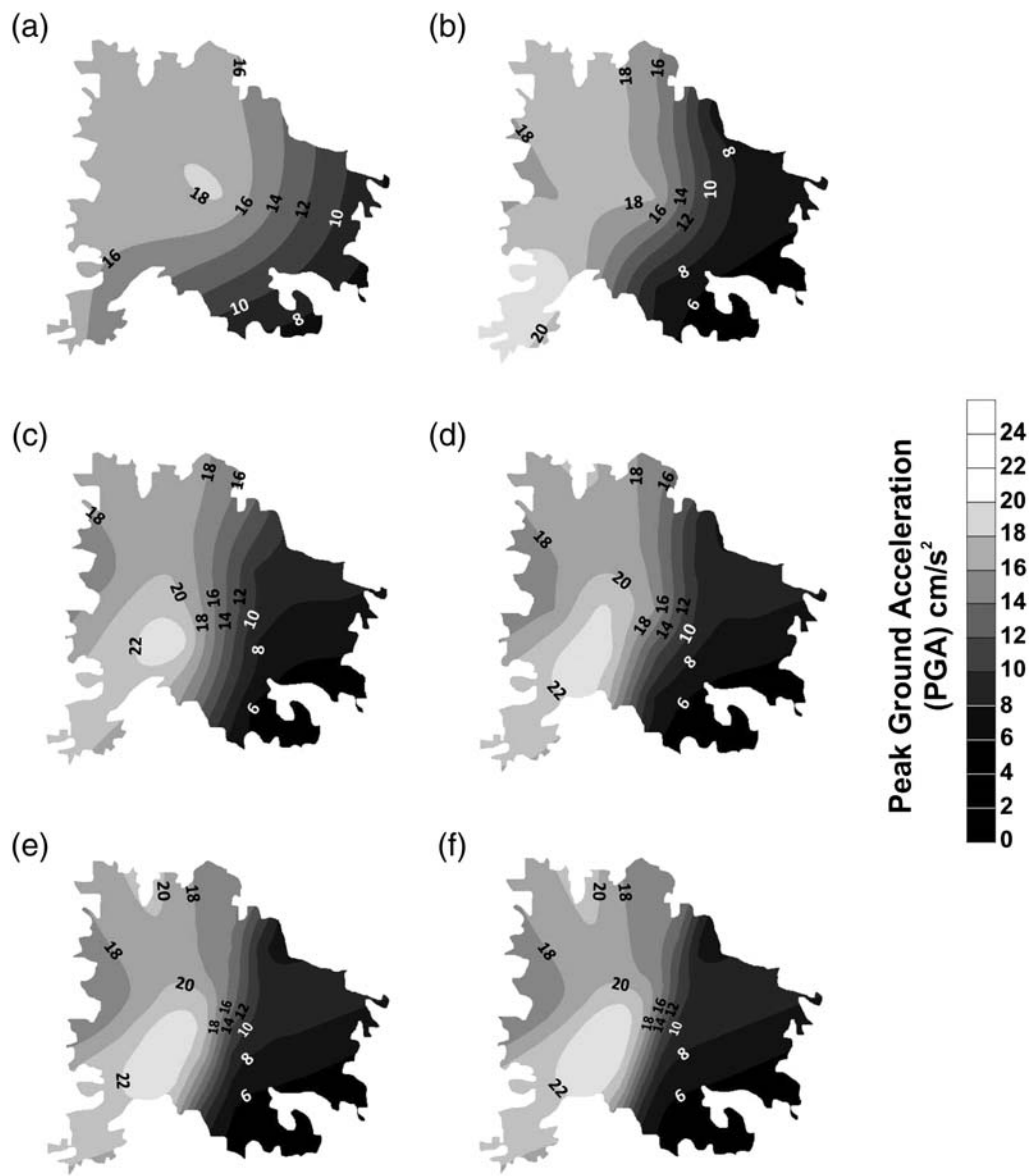
Figure 31.   (a–f) Estimated PGA iteration patterns in the N–S direction obtained for Guadalajara for the M_w 8 CJ1995 earthquake by applying the proposed RNN procedure (with a distance $k = 0.3$ km; see Fig. 22) to the 10 recorded PGA values in the N–S direction shown in Figure 10. (The PGA value of station ROT was used to verify the RNN training results.)

thicknesses $h \leq 20$ m and $h > 20$ m, of its sandy soil layers to competent basaltic rock (see Fig. 2). The latter observation agrees with the results for the important local site effects of Guadalajara superficial sandy soil layers with thicknesses to the basaltic rock of $h > 20$ m, compared with those layers with $h \leq 20$, as discussed in earlier in this section (Number 2).

8. Based on these results, we believe that the hybrid technique to obtain broadband synthetics proposed by Chavez *et al.* (2011) and the proposed RNN methodology can be used to obtain estimates of the seismic hazard in Guadalajara due to the occurrence of M_w 8+ scenario earthquakes in the CJ region, such as the one that occurred on 3 June 1932. This objective will be pursued in a future study.

9. Further improvement in future hazard estimates for Guadalajara (the second largest city in Mexico), especially for M_w 8+ earthquakes, depends on the urgent redeployment and expansion of Guadalajara's accelerographic network. The network operated from 1992 to 1997 and had a 100% success in the recording of the CJ1995 earthquake, but it was shut down due to lack of interest and economic support of local, state, and federal authorities. In addition to its redeployment, we recommend expanding the network to a minimum of 30 recording sites. This action should be accompanied by the necessary geophysical and geotechnical studies at each recording site (such as those performed in the early 1990s; Chavez, 1995), and the necessary economical funds should be provided to operate the network for at least 10 years. This length of time
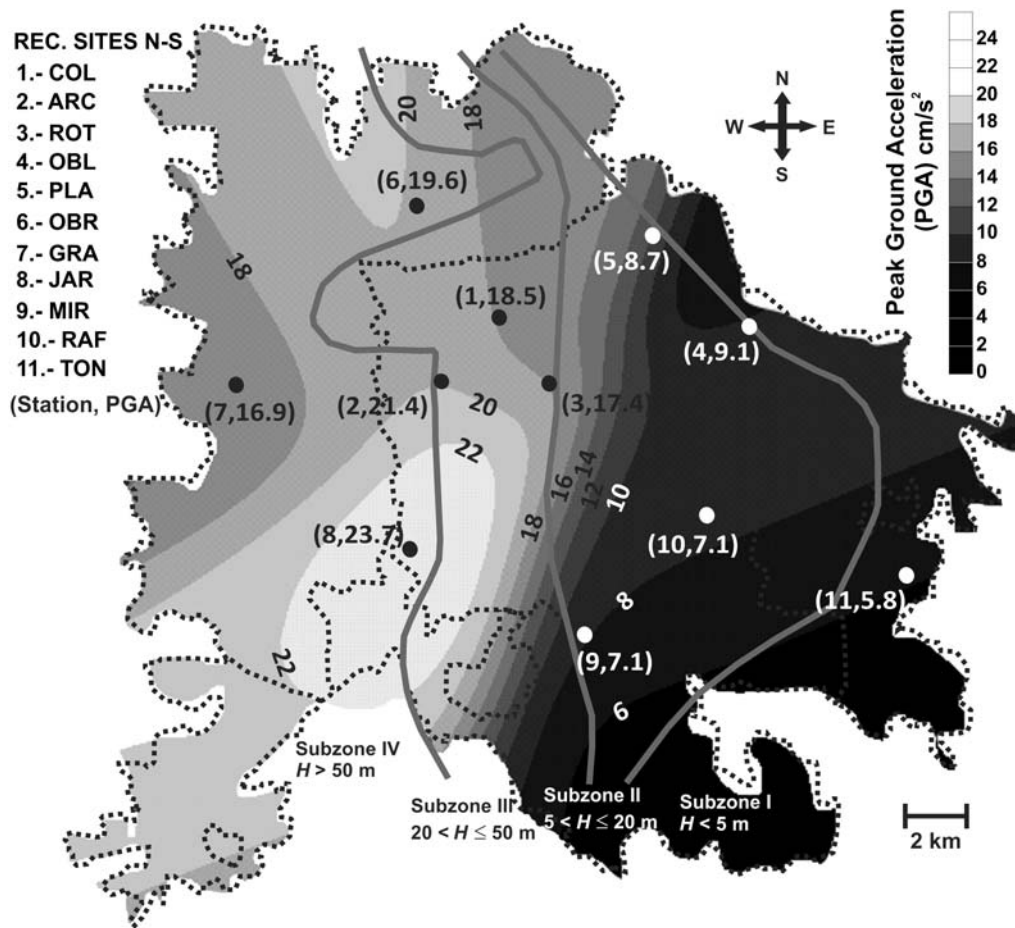
Figure 32.   Estimated PGA pattern in the N–S direction for Guadalajara for the M_w 8 CJ1995 earthquake, obtained by applying the proposed RNN procedure (with a distance $k = 0.3$ km; see Fig. 22) to the 10 recorded PGA values, included beside the black and white dots identifying the recording stations. (The PGA value of station ROT was used to verify the RNN training results.)

is recommended in order to obtain an optimum benefit for the economic investment and to achieve the goal of determining seismic recommendations for Guadalajara that are based on local data, rather than on extrapolations from existing data from other seismically instrumented regions of Mexico or the world. This will eventually lead to a reduction of the seismic risk of Guadalajara's actual built or planned-construction stock.

Data and Resources

We used strong-motion data of Guadalajara's accelerographic network, equipped with Kinemetrics SSA-2 instruments and installed in 1992–1993 (Chavez, 1993, 1995). This network had 11 free-field and two downhole stations (see Fig. 2). The computations (and optimizations) of the 3D finite-difference code used for the 3D low-frequency wave propagation modeling of the 28 September 2004 M_w 6 Parkfield, California, earthquake were carried out using the supercomputers KanBalam of the Dirección General de Cómputo y de Tecnologías de Información y Comunicación (DGTIC)–Universidad Nacional Autónoma de México,

BGQ of the Scientific and Technology Facilities Council (STFC) Hartree Center of the Daresbury Science and Innovation Campus, United Kingdom, and HECToR of the United Kingdom Research Councils.

For the Kolmogorov–Smirnov test, we used the Encyclopedia of Mathematics website, http://www.encyclopediaofmath.org/index.php?title=Kolmogorov%E2%80%93Smirnov_test&oldid=22659> (last accessed November 2013). For the statistics about Guadalajara, we used the INEGI website, www.inegi.org.mx/inegi/default.aspx (last accessed May 2013). For the recurrent network algorithms, we used the Mathworks website, http://www.mathworks.com/index.html?s_tid=gn_logo (last accessed January 2014).

Acknowledgments

References

Bandy, W., V. Kostoglodov, H. Hurtado-Díaz, and M. Mena (1999). Structure of the southern Jalisco subduction zone, Mexico, as inferred from gravity and seismicity, *Geofis. Int.* **38,** no. 3, 127–136.

Campos-Enriquez, J. O., and M. A. Alatorre-Zamora (1998). Shallow crustal structure of the junction of the grabens of Chapala, Tepic-Zacoalco and Colima Mexico, *Geofis. Int.* **37,** 263–282.

Chavez, M. (1993). Red acelerográfica de la zona metropolitana de Guadalajara (RAZMG), *Memorias X Congreso Nacional de Ingeniería Sísmica*, Puerto Vallarta, Mexico, November 1993, 294–300 (in Spanish).

Chavez, M. (1995). Geotechnic, hazard and seismic safety of the Metropolitan zone of Guadalajara, Mexico, Invited opening conference, *X Panamerican Conference on Soil Mechanics and Foundation Engineering*, Guadalajara, Mexico, October 1995, Vol. 4, 33–93.

Chavez, M. (2000). Impact of the local geology on the seismic vulnerability of the Metropolitan zone of Guadalajara, Mexico, *12th World Conference in Earthquake Engineering*, Auckland, New Zealand, 30 January–4 February 2000, CD-Paper 1600.

Chavez, M., E. Cabrera, R. Madariaga, H. Chen, N. Perea, D. Emerson, A. Salazar, M. Ashworth, Ch. Moulinec, X. Li, M. Wu, and G. Zhao (2010). Low frequency 3D wave propagation modeling of the 12 May 2008 M_w 7.9 Wenchuan earthquake, *Bull. Seismol. Soc. Am.* **100,** no. 5B, 2561–2573, doi: 10.1785/0120090240.

Chavez, M., K. B. Olsen, E. Cabrera, and N. Perea (2011). Observations and modeling of strong ground motions for the 9 October 1995 M_w 8 Colima–Jalisco, Mexico, earthquake, *Bull. Seismol. Soc. Am.* **101,** no. 5, 1979–2000, doi: 10.1785/0120100200.

Courboulex, F., S. K. Singh, J. Pacheco, and C. Ammon (1997). The October 9, 1995, Colima Jalisco, Mexico, earthquake (M_w 8): A study of the rupture process, *Geophys. Res. Lett.* **24,** no. 9, 1019–1022.

Custodio, S., P. Liu, and R. J. Archuleta (2005). The 2004 M_w 6.0 Parkfield, California, earthquake: Inversion of near-source ground motion using multiple data sets, *Geophys. Res. Lett.* **32,** L23312, doi: 10.1029/2005GL024417.

Egmont-Petersen, M., D. de Ridder, and H. Handels (2002). Image processing with neural networks—A review, *Pattern Recogn.* **35,** no. 10, 2279–2301, doi: 10.1016/S0031-3203(01)00178-9.

Escobedo, D., J. F. Pacheco, and G. Suárez (1998). Teleseismic body-wave analysis of the 9 October, 1995 ($M_w = 8.0$), Colima–Jalisco, Mexico earthquake, and its largest foreshock and aftershock, *Geophys. Res. Lett.* **25,** no. 4, 547–550.

García, S. R., M. P. Romo, and J. M. Mayoral (2007). Estimation of peak ground accelerations for Mexican subduction zone earthquakes using neural networks, *Geofís. Int.* **46,** 51–62.

García Acosta, V., and G. Suárez Reynoso (1996). *Los Sismos en la Historia de México*, Universidad Nacional Autonoma de México, Fondo de la Cultura Economica, Mexico DF, Mexico (in Spanish).

Graves, A., M. Liwicki, S. Fernandez, R. Bertolami, H. Bunke, and J. Schmidhuber (2009). A novel connectionist system for improved unconstrained handwriting recognition, *IEEE Trans. Pattern Anal. Mach. Intell.* **31,** no. 5, 855–868.

Haykin, S. (1999). *Neural Networks: A Comprehensive Foundation*, 2nd Ed., Prentice Hall, Upper Saddle River, New Jersey.

Hinton, G. E., S. Osindero, and Y. W. Teh (2006). A fast learning algorithm for deep belief nets, *Neural Comput.* **18,** no. 7, 1527–1554.

Hochreiter, S., Y. Bengio, P. Frasconi, and J. Schmidhuber (2001). Gradient flow in recurrent nets: The difficulty of learning long-term dependencies, in *A Field Guide to Dynamical Recurrent Neural Networks*, J. F. Kremer and S. C. Kolen (Editors), IEEE Press, Piscataway, New Jersey, 237–243.

Hopfield, J. J. (1982). Neural networks and physical systems with emergent collective computational abilities, *Proc. Natl. Acad. Sci. Unit. States Am.* **79,** 2554–2558.

Kanamori, H., and D. L. Anderson (1975). Theoretical basis of some empirical relations in seismology, *Bull. Seismol. Soc. Am.* **65,** 1073–1095.

Klitgord, K., and J. Mammericks (1982). Northern east Pacific rise: Magnetic anomaly and bathymetric framework, *J. Geophys. Res.* **87,** 6725–6750.

Kostoglodov, V., and W. Bandy (1995). Seismotectonic constraints on the convergence rate between the Rivera and North American plates, *J. Geophys. Res.* **100,** 17,977–17,989.

Nakamura, Y. (1989). A method for dynamic characteristics estimation of subsurface using microtremor on the ground surface, *Q. Rep. Railway Tech. Res. Inst.* **30,** no. 1, 25–33.

Nishenko, S. P., and S. K. Singh (1987). Conditional probabilities for the recurrence of large and great interplate earthquakes along the Mexican subduction zone, *Bull. Seismol. Soc. Am.* **77,** no. 6, 2095–2114.

Pacheco, J., and N. Kostoglodov (1999). Seismicity in Mexico from 1900 to 1999, http://www.ssn.unam.mx/ (last accessed November 2013).

Serrano, A., E. Soria, and J. Martín (2009). Redes Neuronales Artificiales, Escuela Técnica Superior de Ingeniería, *Tesis de Licenciatura*, Universitat de Valencia, Spain (in Spanish).

Theodoridis, S., and K. Koutroumbas (2008). *Pattern Recognition*, Fourth Ed., Academic Press, Waltham, Massachusetts, ISBN: 978-1-59749-272-0.

Tobler, W. R. (1970). A computer movie simulation of urban growth in the Detroit region, *Econ. Geogr.* **46,** 234–240.

Instituto de Ingenieria
Universidad Nacional Autonoma de Mexico
Ciudad Universitaria
Circuito Escolar s/n
04510 Mexico DF, Mexico
chavez@unam.mx
sgab@pumas.iingen.unam.mx
nperea68@gmail.com
(M.C., S.G., N.P.)

Institute of Advanced Research Computing
School of Engineering and Computing Sciences
Durham University
Higginson Building, South Road
Durham DH13LE, United Kingdom
eduardo.cabrera@durham.ac.uk
(E.C.)

Computing Department
Scientific and Technology Facilities Council
Daresbury Laboratory
Sci-Tech Daresbury
Warrington WA44AD, United Kingdom
mike.ashworth@stfc.ac.uk
(M.A.)

Instituto de Geofisica
Universidad Nacional Autonoma de Mexico
Ciudad Universitaria
04510 Mexico DF, Mexico
alejandrocof@hotmail.com
(A.S.)

Department of Civil and Environmental Engineering
Skempton Building, Imperial College London
South Kensigton Campus
London SW7 2AZ, United Kingdom
erik.chavez07@imperial.ac.uk
    (E.C.)

Departamento de Ingenieria Civil y Topografia
Centro Universitario de Ciencias Exactas e Ingenierias
Universidad de Guadalajara Boulevard
Marcelino García Barragán #1421
esq Calzada Olímpica C.P. 44430
Guadalajara, Jalisco, México
    (J.S.-U.)

City of Toronto
Engineering and Construction Services
Metro Hall, 55 John Street, 20th Floor
Toronto, Ontario M5V3C6, Canada
jsabori@toronto.ca
    (J.S.-O.)